energies

MDPI

Article

The Advanced Control Approach based on SMC Design for the High-Fidelity Haptic Power Lever of a Small Hybrid Electric Aircraft

Aleš Hace

University of Maribor, Faculty of Electrical Engineering and Computer Science, Koroška cesta 46, SI-2000 Maribor, Slovenia; ales.hace@um.si; Tel.: +386-2-220-7301

Received: 2 July 2019; Accepted: 30 July 2019; Published: 1 August 2019

check for updates

Abstract: In the serial hybrid electric propulsion system of a small propeller aircraft the battery state of charge is fluctuating due to the diversity of possible power flows. Overwhelming visual information on the cockpit displays, besides requiring visual pilot attention, increases pilot workload, which is undesirable, especially in risky flight situations. Haptic interfaces, on the other hand, can provide intuitive cues that can be applied to enhance and simplify the cockpit. In this paper, we deal with an enhanced power lever stick, which can provide feedback force feel with haptic cues for enhanced information flow between the pilot and the powertrain system. We present selected haptic patterns for specific information related to the fluctuating battery state of charge. The haptic patterns were designed to reduce pilot workload, and for easy use, safe and energy-efficient control of the hybrid electric powertrain system. We focus on the advanced control design for high-performance force feedback required for rendering fine haptic signals, which stimulates the sensitive haptics of a pilot's hand-arm system. The presented control algorithm has been designed by the sliding mode control (SMC) approach in order to provide disturbance rejection and high-fidelity haptic rendering. The proposed control design has been validated on an experimental prototype system.

Keywords: electric aircraft; hybrid electric powertrain; human-machine Interface; haptics; haptic patterns; kinesthetic haptic interface; haptic power lever; control design; sliding mode control; force control

1. Introduction

Electric vehicles are becoming common, and represent a solution for sustainable transport in the future as well, at least in terms of passenger cars and light transport vehicles [1]; however, electric aircraft are still rather rare, though a strong shift towards electric propulsion aircraft is on the way [2–4]. Some small electric aircraft are commercially available [5], but their flying range is quite limited. A hybrid electric powertrain system [6–9], which combines the propulsion system with an internal combustion engine (ICE) for hybrid electric vehicles, can extend the vehicle's autonomy [10]. A hybrid propulsion concept is being developed for aircraft as well, since it can extend their flying range [11–16].

In an electrical aircraft, an electric motor drives the aircraft propeller. The serial hybrid propulsion system combines two power sources to energize the propeller, batteries, and an ICE. The mechanical energy from the ICE is converted into the electrical energy that powers the electrical motor of the propeller. On the other hand, batteries can also drive the electrical motor of the propeller, if the batteries are not empty. In comparison with a purely electrical aircraft, such a propulsion system can extend the flying range while maintaining low environmental impact and low travel costs. The basic hybrid electric powertrain system architecture is shown in Figure 1. The main system components are a battery pack, an ICE with an electrical generator, and an electrical motor with a propeller. The complex structure of the hybrid electric powertrain requires more information that pilots need to know about it, and, thus, complicates pilot control of the electrical aircraft with the hybrid electric propulsion system. The battery status (state-of-charge, SoC) is an important factor in electrical vehicles [1,17], since it has a significant influence on the vehicle's performance, autonomy and safety. Its impact on safety is even more important in electric aircraft. In the HYPSTAIR project [18], the battery SoC has been identified as key information that must be transmitted to the pilot [16].

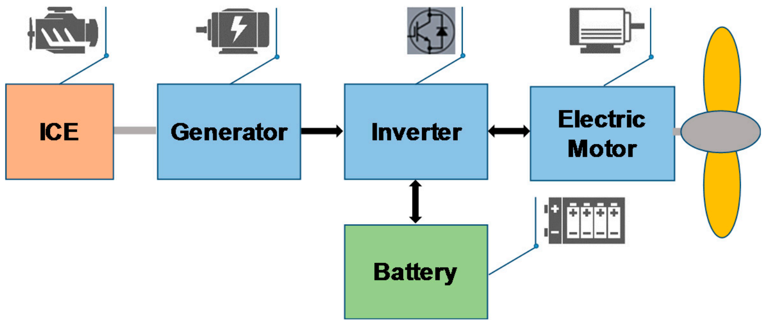

Figure 1. The basic architecture of a serial hybrid electric propulsion system.

As a hybrid electric propulsion system is more complex than a purely electrical or a pure ICE propulsion system, the complexity level of the human-machine interface (HMI) can also become much higher. A pilot receives overwhelming information from the flight deck visual displays that can be burdensome and non-intuitive, and cause a relatively high pilot workload. Thus, aircraft designers are seeking new solutions for cockpit displays that will involve haptics and, thus, simplify piloting [19,20]. Thus, piloting in the case of such a hybrid propulsion system can be more difficult. Consequently, operation with a pilot-in-the-loop may not be optimal. Therefore, the powertrain information should be displayed to a pilot via another communication channel, which can decrease the load for the pilot.

Human haptics refers to the human sense of touch and movement. Humans use haptic sense in interaction tasks for object exploration, movement, and manipulation, and in communication as well [21–29]. A haptic interface is a haptic device that allows for haptic indirect interaction with a real or artificial environment (e.g., [30–33]). It is a mechanical device designed to provide force feedback for human haptics' stimuli, which refers to the information transmitted by kinesthetic interaction. The use of haptic interfaces in teleoperation, robotics, and computer technology has been well known for a few decades [26,34–38]. Recently, new haptic applications have appeared in different areas, such as human assistance systems and medicine [39–43].

Mechanical controls in cars such as a steering wheel, a gas pedal, and a gearshift, have been converted into specific haptic interfaces, and integrated in steer-by-wire, drive-by-wire control systems, or advanced driver assistance/support systems [44–56]. In aircraft, the fly-by-wire approach integrates mechanical control inceptors such as sticks, yokes, or rudders [57–60]. However, the wired electronics control technology overrides the natural mechanical feedback. In order to overcome this problem, the redesigned mechanical controls must provide proper artificial force feedback to stimulate human kinesthetic sensations; thus, active haptic inceptors have been developed recently [61–63]. Furthermore, this can be supplemented with an additional set of haptic stimuli, which can communicate to the human operator various other information related to the operational system state and environment, in order to assist him/her in control and to improve situational awareness, safety, and performance [64–68]. High-fidelity force feedback driven by complex mathematical models is required for a more authentic response and engaging user experience.

Kinesthetic haptic interfaces provide information exchange by force and motion [69,70]. Haptic interfaces may be implemented by different control schemes [22,34,71–73]. An impedance control approach is a key technology in force/motion control for any mechanical system in constrained motion [74] and, thus, it is applied widely when a mechanical system interacts with a human. In [75] the authors proposed adaptive impedance control for a force-feedback haptic interface system in order to deal with dynamic changes of a human musculoskeletal system and enhance human skill on a haptic interface system. In [76], the authors implemented impedance control for a therapeutic exoskeleton for upper limb rehabilitation training. However, the impedance control schemes are difficult to implement in haptic interfaces: If a desired impedance is to be enforced, then the interface mechanism's own dynamics must be compensated. The interface mechanism inevitable involves friction. Friction is a natural phenomenon, which is difficult to model and to override [77–85]; impedance haptic interfaces are, by nature, lightly built and highly back-drivable [22], and thus also more safe, which may be an extremely important design factor. Such haptic interfaces can provide implementation of vivid haptic patterns and good performance in terms of a wide impedance range and force resolution [22,72,86]. If high performance is required, a closed-loop control should be applied, which can reject disturbances robustly, especially in back-drivable systems, which are subjected to a full direct load on the motor axis. Thus, we can achieve good haptic fidelity.

The control algorithm for a high-fidelity haptic interface must be robust against disturbances and uncertainties, which include friction, inertia modeling errors, and neglected parasitic dynamics. Though the obvious source of these is the mechanism of the haptic interface itself, another significant disturbance is the interaction with the pilot's own impedance [57,73,87,88]. The erroneous control model demands a robust control law. The sliding mode control (SMC) design approach may be utilized to improve robustness in feedback control considerably [89]. Thus, we can find numerous applications of sliding mode control in many areas, such as: control of a parallel robotic manipulator with uncertain dynamics [90], bilateral control of a hydraulic manipulator [91], control of a therapeutic exoskeleton [76], an electronically controlled power steering system [92], steer-by-wire systems [47], an automotive electronic throttle [93], robust speed control of PMSM [94], position control of a synchronous reluctance motor [95], a PEM fuel cell power system [96], etc. The basic SMC is characterized by a variable structure system and switching of the control input variable [97]. Though the switching control was originally introduced to guarantee robust stability, it usually leads to chattering in practical systems [98]. The chattering is an undesired oscillation phenomenon. Therefore, in practical mechatronic systems, in which the control input can only be a continuous function of time, sliding mode controller design could be a challenging task. In order to prevent chattering, the robust control must be smoothed somehow. One approach to eliminating chattering caused by discontinuous control has been introduced by a higher-order sliding mode control [99], which preserves robustness; however, the relative degree between the sliding variable and the control variable is increased proportionally. In [100], the authors proposed a dynamical controller by passing discontinuous control action onto a derivative of the control input. The most famous is the super-twisted algorithm, which belongs to the class of second-order SMC [101]. However, recent research related to its practical implementations shows that it can still produce a chattering phenomenon in some cases [102]. Thus, an alternative approach has been presented in [103]: The impedance control scheme for robot manipulators has been derived by the SMC design procedure (similar to [100]), resulting in continuous control, which preserves fair robustness while preventing chattering. The proposed control design concept has then been implemented successfully in different practical applications [104–107].

In this paper, we propose the control design of a haptic power lever for a hybrid electric aircraft with force feedback features that supplement visual information with haptic information, since the human response to physical cues (pressure, force) is much faster than the response to the visual observations. The haptic power lever was designed conceptually with an ambition to provide reliably relevant information about the hybrid propulsion system by intuitive "natural-like" haptic patterns such as friction, constant return force, bump, and graininess, in order to simplify piloting of the small hybrid electric aircraft. The haptic cues aim to provide intuitive control by communicating information via human haptics. We believe that such an approach enables a significant reduction of the pilot workload, increases the pilot's awareness of the batteries' use and prolongs their life, and optimizes control of the complex hybrid electric powertrain system and energy use. We focus on a robust control algorithm for the power lever designed as a haptic interface, aiming to render fine haptic patterns at the highest possible fidelity, which presents the main contribution. Therefore, we apply the concept of the SMC design procedure [103] for the derivation of the chattering-free control algorithm, similar as in [108]. However, in this paper, force regulation has been achieved via a desired impedance, which is enforced to the haptic interface. The optimized control algorithm, including the designed haptic patterns for a single impedance haptic interface, have been implemented practically. The implementation highlights of the advanced control design also involve a precise measurement of position, and especially velocity, which is required for high-performance haptic applications [109,110]. We show a simple experimental prototype of the haptic power control lever, which demonstrates high-quality rendering of the proposed haptic patterns. The presented experimental results verify the proposed control design.

The rest of the paper is organized as follows: Firstly, we show the main concept of the hybrid electric powertrain system control via human haptics in Section 2.1. Then, in Section 2.2, we explain the complex human haptics, and provide a biomechanical model of a human arm required for the consideration in the control design. In Section 2.3, we present the proposed haptic patterns that a pilot should feel in relation to some important information sourced by the powertrain system. In Section 2.4, we show the detailed derivation of the control algorithm for the haptic interface. The experimental system is presented in Section 2.5. Then, the experimental results are shown in Section 3, to verify the effectiveness of the proposed algorithm, which is followed by the discussion in Section 4. Finally, Section 5 concludes the paper.

2. Materials and Methods

2.1. The Main Concept of the Powertrain System Haptic Control

In the serial hybrid electric propulsion system (see Figure 1) the electrical motor, which drives the propeller, is powered by the electrical generator, which is driven by the ICE; the battery pack presents an additional energy source. There are many possible power flows in such hybrid electric powertrain system, as depicted in Figure 2.

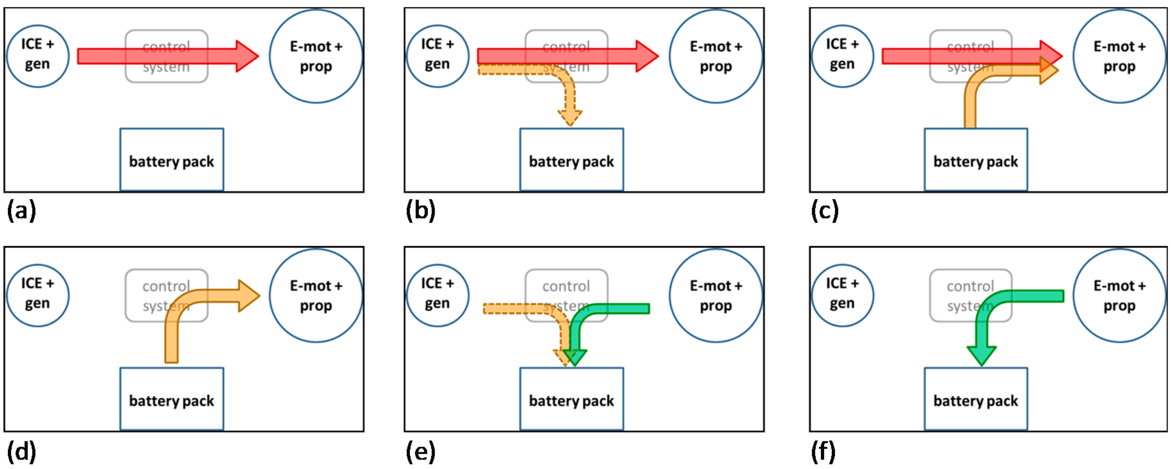

Figure 2. Some possible power flows in the serial hybrid electric propulsion system: (**a**) The ICE with the generator powers the propeller electrical motor directly; (**b**) the same as (a) plus the ICE with the generator charges the battery pack; (**c**) both the ICE with the generator and the battery pack power the propeller electrical motor; (**d**) the battery pack solely powers the propeller electrical motor; (**e**) the battery pack is charged by the propeller electrical motor and by the ICE with the generator in the regeneration regime; (**f**) the battery pack is charged solely by the propeller electrical motor in the regeneration regime.

In case of low power demand, the propeller is driven solely by the ICE. It may also charge the battery pack. At a high power demand, the battery pack powers the propeller as well and then the batteries deplete. The propeller may also be driven solely by the battery pack. The propeller may also charge the battery pack in the regeneration regime. It is very important that the pilot can have available power when it is required for flying, e.g., in the case of taking-off, climbing, and other demanding maneuvering, although high power will be available only from the batteries. The ICE can deliver only low power. This means that the state-of-charge of the battery pack is very important for safe flight, and the pilot must be aware of it all the time.

The general operation concept and the basic system structure of the hybrid electric aircraft with the haptic power lever and a pilot-in-the-loop is presented in Figure 3. The pilot operates the powertrain system by manipulating the power lever, which is wired to the HMI control unit. The relevant system data are converted to haptic patterns in the feedback, thus stimulating haptic mechanoreceptors of the pilot's hand–arm system. Hence, audiovisual information is complemented by haptic signals.

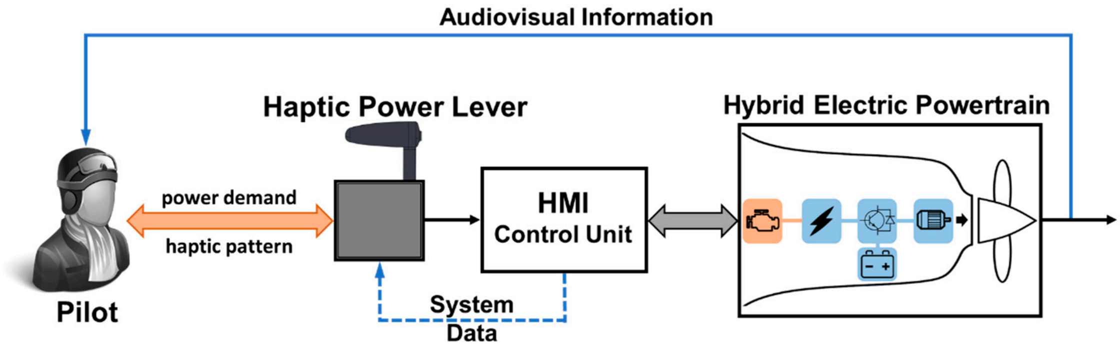

Figure 3. Pilot feedback involves audiovisual information and haptic information delivered by the force feedback of the haptic power lever.

Haptic-based system control should be intuitive, and then the pilot's workload can be reduced significantly. The information flow between the human operator, i.e., the pilot, and the system, i.e., the aircraft powertrain, is presented by the block scheme depicted in Figure 4. The pilot provides a power demand for the aircraft powertrain system by positioning the power lever. Simultaneously, he or she can receive force feedback, which is linked to the information from the aircraft powertrain system. The force feedback is related to the haptic patterns produced by the haptic power lever. The control system of the power lever converts the position to the power demand, and the powertrain system state is converted to physical force that provides haptic information. Thus, the information flow is bidirectional: In one direction we provide system control, and in the other we provide system information.

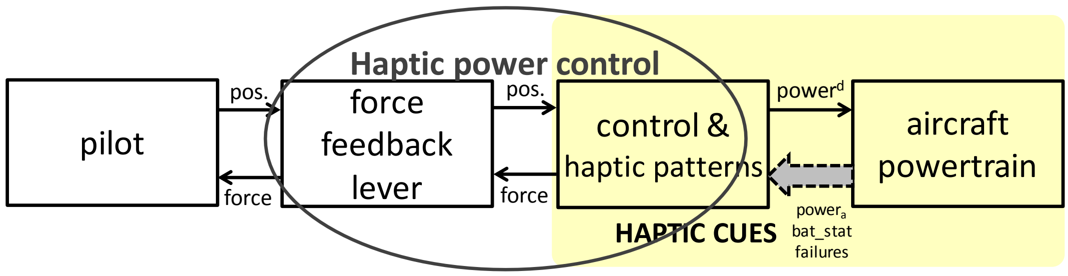

Figure 4. The concept of the powertrain control and haptic information flow with pilot-in-the-loop.

Haptic signals are related to haptic patterns and haptic cues. Haptic patterns refer to emulation of a natural contact feel or generating artificial feel. Haptic cues are haptic patterns that are linked to higher-level information. In our case, the haptic patterns are linked to the powertrain system state information. We have designed the haptic power lever with a natural-like force feel (i.e., a feedback force that we can feel in nature while touching objects), which should generate an effective haptic stimulus. The patterns such as friction, graininess, and constant force feedback, have been adopted in our design, to provide the pilot with intuitive information. These have been designed with the aim to enable detection, discrimination and identification the relevant information of the hybrid electric powertrain system. In the sequence, this should further enable proper and intuitive decision making of the pilot. Thus, the haptic information will help the pilot in flying performance and increase safety.

The force felt by a pilot is generated by various haptic patterns. The selection of the proper haptic patterns is based on the power demand ("power^d") and the state information of the aircraft's powertrain system, which includes available power ("power$_a$"), battery status ("bat_stat"), and failures. The pilot should feel the selected haptic pattern while moving the power lever. When the propeller is driven solely by the ICE, then the pilot should feel friction of a low level. When the batteries deplete, then the pilot should feel friction of a high level. When passing from a low power demand to a high power demand (or vice versa), a bump shall be generated, to inform the pilot about crossing the border. In the case of a high power demand beyond available, the constant return force pattern of a very high level should be felt by the pilot. The haptic power lever should supplement the friction pattern with a graininess in the case of low or empty batteries. If the pilot is decreasing the power demand and regeneration of the batteries occurs, then the friction pattern of a very low level should be felt by the pilot. In this case, when moving the power lever backward, a light bump should generated to inform the pilot about entering into the regeneration mode.

2.2. Human Haptics and the Biomechanical Model of a Human Arm

The human haptic system is rather complex. Its complex structure can be divided into the following components: the mechanical component, the sensory component, the motoric component and the cognitive component [21,22,26,27,34]. The most important part of the mechanical component is the arm-hand subsystem. The sensory system includes large numbers of various receptors and nerve endings. Tactile mechanoreceptors, which enable the human sense of touch, are located in the skin. Kinesthetic mechanoreceptors are located in joints, tendons, and muscles. They allow perception not only of force/torque in our muscles, but also the operational state of the human locomotor system. Humans perceive haptic signals dynamically. Though human haptic perception goes up to a frequency of 10 kHz, the highest sensitivity is between 100 Hz and 1 kHz. Static components prevail in the dynamics. Human haptic sense can evidently be broken down into the low-frequency, high-power kinesthetic interaction channel and the high-frequency, low-power tactile perception. The first is the most important for the design of a kinesthetic haptic interface. Power grasps are designed for strength and stability, involving the palm, as well as the fingers. Maximum forces can be in the range of 5 to hundreds of Newtons [111].

Besides the dynamical properties of haptic perception, a mechanical model of a human arm and hand, which grasps the interface effector, is of high importance in the mechanical and control design of the haptic interface. Obviously, the exact modeling of the human arm is still a complex problem [21]. We can find many different biomechanical models in the literature for passive human response [112–115]. In general, a simplified biomechanical model can be represented by a passive impedance, i.e., the force-velocity relationship Z_h = force/velocity. In an alternative formulation of the human impedance, velocity can be replaced by position, i.e., Z_h = force/position. Then, this simple model is usually given by the impedance of the second order:

$$Z_h(s) = m_h s^2 + b_h s + k_h, \tag{1}$$

where m_h, b_h and k_h denote mass, damping and stiffness, respectively. These parameters' values can only be estimated by a certain degree of speculation [22]; thus, they are found experimentally to be very different: (a) m_h = 11.6 kg, damping b_h = 17 Ns/m, and stiffness k_h = 243 N/m [112], or (b) m_h = 17.5 kg, damping b_h = 175 Ns/m, and stiffness k_h = 175 N/m [113], or (c) m_h = 3.25 kg, damping b_h = 20 Ns/m, and stiffness k_h = 300 N/m [114]. A simplified dynamic representation reduces to a two-parameter spring-damper model with stiffness and damping; however, in order to better approximate the linear dynamics in the low-frequency domain below 20-30 Hz, Speich et al. [115] developed a five-parameter model, which supplements the basic second-order arm dynamics with an additional spring-damper model for hand dynamics. The eight-parameter model, which includes elasticity and damping of the skin (with tissue) being in direct contact with the end-effector (handle), and finger/hand/limb dynamics, has also been developed for frequencies beyond 20 Hz [21]. However, all these parameters are very uncertain and can have a large range, since they vary from person to person, and are based on how the end-effector of the haptic interface is held by the human hand. They may also vary at each instant in the limb trajectory. Additional variations in the parameter values can be observed if we consider the three-dimensional motion of a dexterous and reconfigurable human arm [116]. The dynamics are even more complicated when we consider a human coupled with a haptic device—then structural flexibility, different grasping conditions, and active human stabilization with reflex delay must be taken into account as well [117]. Humans vary the impedance of their limbs significantly by the neuromuscular system during many manipulation tasks and during interaction with their environment in order to reduce contact forces, to increase positional control, and to stabilize unstable dynamics [88]. Thus, besides the human neuromuscular system, other factors, such as human haptic perception, the cognition process and motor control system, also determine the active human response [87].

2.3. Haptic Patterns

The implementation of the proposed haptic patterns is based on mathematical formulas or algorithms, as follows.

2.3.1. Friction

Friction is a complex natural phenomenon arising at the contact of surfaces, thus, there are many different models in the literature. However, there is still a lack of a single perfect mathematical description that could be used for a highly realistic simulation [77,78,80,84,118]. We consider friction as the force that resists the relative motion of solid surfaces sliding against each other. Such friction is dry friction, which includes several components, such as static friction or stiction, and kinetic friction. Stiction appears between static surfaces, whereas kinetic friction occurs between moving surfaces. In the static case, the opposing force to the friction matches the applied external force if it is less than some threshold value, and relative motion cannot occur. The transition from the stationary state to motion may result in the so-called stick-slip effect [86]. In sliding motion, kinetic friction occurs, which is typically further subdivided into the Coulomb friction component, the viscous friction component, and the Stribeck effect friction component. The Coulomb friction relates to the normal force applied on the surface. It is independent of the sliding velocity, and, thus, it is usually considered to result in a constant force at any velocity; however, in practical mechanical systems it can fluctuate as well, e.g., due to changes in the normal force. The viscous friction appears in many mechanisms with lubrication to reduce friction and wear. It is proportional to the relative velocity. The Stribeck effect friction is the component of the friction force that originates at very low sliding velocities, and has negatively sloped characteristics in relation to the relative velocity. Kinetic friction always resists motion. When the direction of motion is changed with the transition through zero velocity, the direction of the opposing force of friction is changed instantly.

Typical mathematical models of friction are based on a discontinuous function with switching at zero velocity related to the Coulomb friction component, and, thus, this presents a hard nonlinearity. To represent the stiction effect in the stationary case of zero velocity, the direction and value of the applied external force must also be taken into account. Such mathematical models are, therefore, a difficult task for digital computer simulation of body motion with friction [119]. Additional problems related to detection of zero velocity (and sensing accurate velocity as well) appear in haptic interfaces, which implement digital encoders for position sensing. The finite velocity resolution presents a serious problem for fidelity of haptic rendering in real applications [110]. Thus, there are numerous attempts to alleviate numerical computation problems related to discontinuities at zero velocity. The Karnopp friction model [77] extends the zero velocity point to a narrow band around which the velocity is considered 0, whereas the friction force is calculated to be the smallest value of either: (a) The value required to keep the system at zero velocity, or (b) The stiction force level. Although this model is rather simple, it captures important features of real friction, including explicit representation of stiction and treatment of the transition between low velocities and static contact, and, thus, represents a good candidate for a natural-feel friction model. Furthermore, it circumvents the low-velocity resolution issue with the velocity threshold introduced by the narrow band around the zero velocity point. Thus, the authors in [119] proposed the Karnopp model with viscous friction for optimal haptic rendering depicted in Figure 5, which we have also adopted in this paper; it is described mathematically as follows:

$$F_f(v, F_a) = \begin{cases} -F_c + b_v v, & v < -\delta v \\ \max(-F_s, F_a), & -\delta v \le v < 0 \\ \min(+F_s, F_a), & 0 < v \le \delta v \\ +F_c + b_v v, & \delta v < v \end{cases}, \tag{2}$$

where F_f, F_a, F_s, F_c stand for the friction force, the applied force, the stiction, and the Coulomb force, respectively; v is the velocity, δv determines the width of the near-zero velocity band (the velocity below δv is considered zero), and b_v is the viscous friction coefficient. In general, the applied force F_a incorporates all non-frictional forces applied to the system. The sliding phase occurs when the velocity relative to the object surface exceeds the predefined minimal velocity $|v| > \delta v$. Friction in this phase consists of the Coulumb friction component (i.e., $\pm F_c = F_c \cdot \mathrm{sgn}(v)$) and the viscous friction component (i.e., $b_v v$) that is proportional to velocity. The sticking phase occurs when the velocity relative to the object surface is smaller than the minimal threshold velocity $|v| \le \delta v$. Then, the system is in a stuck state.

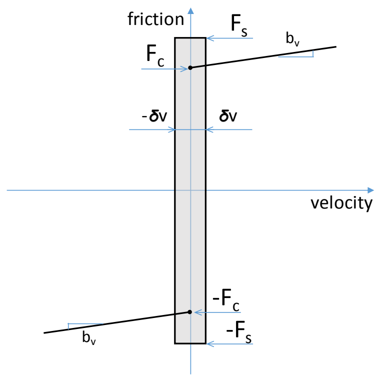

Figure 5. The Karnopp friction model for haptic rendering.

The Karnopp model is numerically simple and, therefore, its implementation for haptic rendering should be rather simple. In the sliding phase, the friction is a function of velocity, whereas in the stuck state, the friction is a function of the applied force. However, when this is to be implemented on a real haptic interface, some hardware related factors should be considered, since, besides measurement of velocity, it also requires measurement of applied force for determining the opposing force in the stationary stuck state. Due to the hardware limitations related to uncertain measurement of the applied force (which includes real sensor characteristics, such as resolution, noise, nonlinearity, etc.), real actuator dynamics, and finite sampling frequency, an exact replica of the friction model (2) is impossible; especially in the sticking phase, rendering of the opposing static friction, which must match the applied force to guarantee stationary state when $|F_a| < F_s$, is a problem. Therefore, we wish to avoid a direct involvement of the applied force in friction rendering. Nevertheless, rendered friction should resemble the natural friction as much as possible. Thus, we should put special emphasis on the implementation of the stuck phase (pre-sliding phase) and the soon-after-break-away phase (transition from stuck state to sliding, i.e., stick-slip phase). A good approach to deal with this problem is the introduction of a virtual spring [34,119], whose role is to convert the motion to a force by the impedance causality. The virtual spring is attached in the so-called stuck position. The stuck position (x_{stuck}) refers to the position (x) during sliding in which the velocity just below the minimal value is first detected ($x_{stuck} = x$ at $v \leq \delta v$ in sliding). It is the position assigned to represent where the system entered the stuck state. When velocity falls below the minimal value, the sliding phase switches to the stuck state. In the stuck state, the virtual spring force defined by

$$F_{vs} = K_{vs}(x - x_{stuck}), \tag{3}$$

where K_{vs} represents the virtual spring stiffness (related to the so-called frictional stiffness), somehow measures or estimates the applied force ($F_a \approx F_{vs}$), since even very small deviation from the stuck position will result in a force proportional to this position deviation. Thus, the virtual spring force may replace the applied force in (2). Accordingly, from the hardware implementation point of view, measurement of the applied force may be replaced by a measurement of position, though it should be precise enough to capture the very small position deviation in the stuck state. The detailed algorithm is presented in [119].

2.3.2. Bumps

Bumps are relatively simple. These relate to the geometrical shape of a small hill on a surface. While moving a hand over a bumpy surface, we feel force whilst crossing the small hill. The problem of haptic rendering in this case relates to virtual textures [120]. A founding work in haptic rendering related to this problem was by Minsky [121], who showed that textures and surface features can be represented by lateral force fields. Also, rendering larger-scale surface features such as bumps or holes by a haptic manipulandum has later been shown to be possible by the method of lateral force fields; it has been shown that force cues (not geometric cues) determine the shape perceived by haptics [122,123]. The method of lateral force fields generates forces whose magnitudes are proportional to the slope of a position function that defines the virtual surface feature.

A single-dimensional rigid virtual haptic bump geometry can be described by a Gaussian function:

$$y_b(x) = A_b \cdot \exp\left(-\frac{(x - p_b)^2}{2w_b^2}\right), \tag{4}$$

where x, p_b, w_b, y_b, A_b are lateral positions on the surface, a center position of the bump defining its peak, the bump width measure, current height of the bump, and the maximum height of the bump, respectively. The method of the lateral force field determines the feedback force during crossing the bump by the gradient:

$$F_b(x) = K_b \frac{dy_b(x)}{dx}, \tag{5}$$

where K_b is some constant to be defined. Here, the slope of the bump resists the lateral movement while climbing up. The steeper the bump, the stronger the resistance. The bump force Equation (5) equates to

$$F_b(x) = K_b \frac{dy_b(x)}{dx} = -\frac{x - p_b}{w_b^2} K_b A_b \cdot \exp\left(-\frac{(x - p_b)^2}{2w_b^2}\right). \tag{6}$$

It is easy to analyze Equation (6) for the function extremes. They are achieved at the inflection points when $x = p_b \mp w_b$. Then we get peak forces as $F_b^{peak}(x = p_b \mp w_b) = \pm K_b A_b \cdot \exp(-\frac{1}{2})/w_b$. Thus, if we choose

$$K_b = F_b^{\max} \frac{\exp(\frac{1}{2}) w_b}{A_b}, \tag{7}$$

where $F_b^{\max}$ stands for the maximum bump force, then Equation (6) can be rewritten as

$$F_b(x) = -F_b^{\max} \frac{x - p_b}{w_b} \exp(\frac{1}{2}(1 - \frac{(x - p_b)^2}{w_b^2})). \tag{8}$$

The bump, along with the associated force, is illustrated in Figure 6. Here, we have assumed default values of the bump parameters (i.e., $p_b = 0$, $w_b = 1$, $A_b = 1$, $F_b^{\max} = 1$) and the manipulandum travels in the positive direction of the lateral position increase. At the bump peak, the bump force is 0, the maximum force is achieved at $x = p_b \mp w_b$, whereas close to the bump position boundaries $x = p_b \mp 3w_b$ the bump height is about 1.1% of its maximum, while the bump force is only around 5.5% of the peak value.

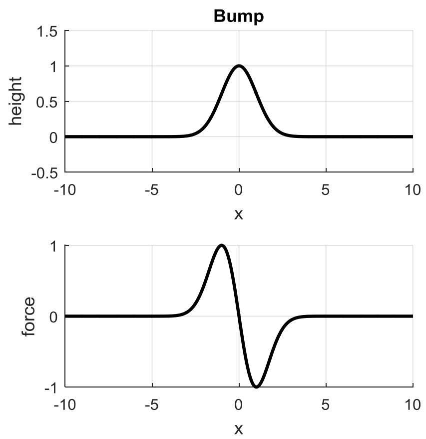

Figure 6. Illustration of the bump force model.

2.3.3. Graininess

We consider graininess similar to surface roughness. Therefore, the problem is related to virtual textures. Only coarse grain is relevant for our purpose. Since, in the presented design, we consider that it is not constrained strongly to any natural shape, we use a very simple artificial graininess force rendering formula:

$$F_g(x) = F_g^{\max}\left(1 + \sin(2\pi \frac{x}{w_g})\right), \tag{9}$$

where x, w_g, F_g, $F_g^{\max}$ are lateral positions on the surface, the grain width, the grain force, and its maximum value, respectively. The model of this artificial surface texture profile with graininess is related to the cosine function of the lateral position, while the corresponding force to be rendered is biased in order to avoid the pulling effect. The graininess is illustrated in Figure 7. Here, we have assumed default values of the grain parameters (i.e., $w_g = 1$, $F_g^{\max} = 1$) and the manipulandum travels in the positive direction of the lateral position increase.

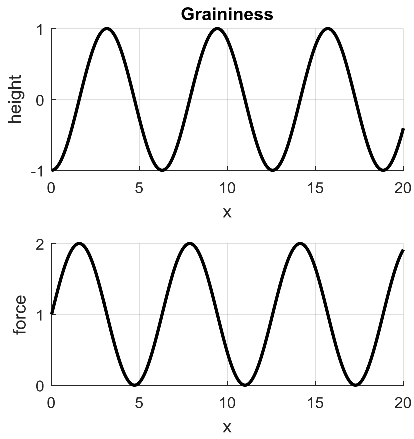

Figure 7. Illustration of the graininess force model.

2.3.4. Constant Return Force

The constant return force (CRF) is the simplest haptic pattern considered in our study. It is only able to generate force with a constant level such that it is felt in the negative direction.

2.4. The Control Algorithm for the Haptic Interface

2.4.1. The Dynamic Model of the Haptic Interface

We consider a haptic interface with a single degree-of-freedom (DOF) mechanism, which enables linear motion of the end-effector handle. The mechanism is driven by a linear servo motor. It is responsible for generating a feedback force that is to be felt by a human holding the manipulandum handle. The motion equation can be written as

$$m_m \cdot \ddot{x} + f_f + f_g = f_m - f_h, \tag{10}$$

where x, f_f, f_g, f_m, and f_h denote motor position, friction force, gravity force, motor force and human force. m_m is a lumped mass of the mechanism moving part. The passive biomechanical human dynamics, which we consider to result in the force f_h, is given by Equation (1). The friction force and the gravity force can be regarded as a disturbance force f^{dist} acting on the system. Typically, the disturbance may also involve model uncertainties and perturbation. However, Equation (10) can be rewritten as

$$m_m \cdot \ddot{x} + f^{dist} = f_m - f_h. \tag{11}$$

The basic block scheme of the haptic interface coupled with a human is presented in Figure 8.

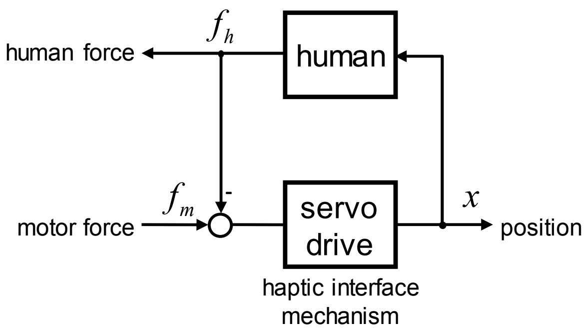

Figure 8. The basic system block scheme for control design of the haptic interface.

2.4.2. The Impedance Control

The impedance control approach [124–126] is employed when a mechatronic device is in contact with its environment or with a human. It is an important control concept in modern robotics that is demonstrated by numerous applications [127–140]. The mechanical impedance, which features a force response of a body or a system of bodies on imposed velocity or position, can be described as a force-velocity relationship or force-position relationship. It can be given in a second-order simple linear form

$$\frac{F(s)}{X(s)} = Z(s) = ms^2 + bs + k, \tag{12}$$

where s is the complex Laplace variable, and $F(s)$, $X(s)$ and $Z(s)$ are the force, the position, and the mechanical impedance in the complex Laplace domain, respectively. The impedance parameters m, b, and k stand for mass inertia, damping and stiffness, respectively.

The impedance control enables compliance in constraint motion and force regulation. A typical control goal is to enforce a desired impedance characteristic to a robotic mechanism with its own nonlinear impedance. If we consider the mechanism in contact with its environment, then the desired impedance may be described in the time domain:

$$m^d \cdot \ddot{x} + b^d \cdot \dot{x} + k^d \cdot x = f^r - f_e, \tag{13}$$

where x, f_e and f^r are the position, the reaction force in the contact with an environment, and the reference force, respectively. m^d, b^d, and k^d stand for desired mass inertia, desired damping and desired stiffness, respectively.

Typically, we consider the environment with the impedance Z_e such that

$$F_e(s) = Z_e(s)X(s). \tag{14}$$

If we assign the desired impedance Z^d for the robot mechanism as

$$Z^d(s) = m^d s^2 + b^d s + k^d, \tag{15}$$

and consider a physical interaction between the mechanism and the environment such that we can rewrite Equation (13) as

$$Z^d(s)X(s) = F^r(s) - F_e(s), \tag{16}$$

then by combining Equations (14) and (16) we can derive the expression that determines the interaction force:

$$F_e(s) = \frac{Z_e(s)}{Z^d(s) + Z_e(s)} F^r(s). \tag{17}$$

If we consider the second-order environment impedance,

$$Z_e(s) = m_e s^2 + b_e s + k_e, \tag{18}$$

then Equation (17) reads in the time domain as

$$(m^d + m_e)\ddot{f}_e + (b^d + b_e)\dot{f}_e + (k^d + k_e) f_e = m_e \ddot{f}^r + b_e \dot{f}^r + k_e f^r. \tag{19}$$

In the case of an asymptotically stable interaction, the environment force after the transient period in the steady state can be derived as follows:

$$f_e^{ss} = \frac{k_e}{k^d + k_e} f^r. \tag{20}$$

Obviously, if the desired stiffness of the robotic mechanism is 0 ($k^d = 0$), then the steady-state contact force matches the reference force perfectly $f_e^{ss} = f^r$. In this case, the steady-state position is $x^{ss} = f^r/k_e$. If, further, the reference force is 0 $f^r = 0$, then $x^{ss} = 0$, and the robotic mechanism is fully compliant.

In our case, the haptic interface mechanism is coupled with the human, which is modeled by the passive biomechanical impedance in Equation (1). We wish to produce haptic patterns as described in Section 2.3, in which they are designed for certain force feels. The haptic interface should provide the force following the reference generated by a haptic pattern. Therefore, we prescribe the desired impedance for the haptic interface as

$$Z_m^d(s) = m_m^d s^2 + b_m^d s, \tag{21}$$

where m_m^d and b_m^d are desired mass and desired damping, respectively, and their values can be chosen arbitrarily. Considering Equation (21), we can rewrite Equation (17) and then obtain the transfer function:

$$\frac{F_h(s)}{F^r(s)} = \frac{Z_h(s)}{Z_m^d(s) + Z_h(s)} = \frac{m_h s^2 + b_h s + k_h}{(m_m^d + m_h)s^2 + (b_m^d + b_h)s + k_h}. \tag{22}$$

We wish to enforce dynamics such that the apparent mass and the apparent damping will show the haptic interface as a lightweight ($m_m^d \to 0$) mechanism with low friction ($b_m^d \to 0$) as much as possible. If necessary, the desired damping may be used for stabilizing the interaction [86,117,141–144]. However, in an ideal case, the transfer function converges to 1, and the feedback force may match the reference force generated by a haptic pattern perfectly. Of course, this is a highly non-realistic scenario, since it assumes that the control can compensate for the dynamics of the mechanism perfectly, which is impossible in practice.

2.4.3. Derivation of the Control Algorithm

Chattering-Free SMC Design

We represent the control plant by the following state space form:

$$\dot{z}_j = z_{j+1}, \dot{z}_n = f(\mathbf{z}) + b(\mathbf{z})u - d, \tag{23}$$

where $j = 1, \ldots, n-1$, $\mathbf{z} = [z_1, \ldots, z_n]^T$ is a system state vector, u is a scalar control input and d is an unknown disturbance. $f(\mathbf{z})$ and $b(\mathbf{z})$ are considered as nonlinear functions of the system states, respectively.

The goal of the SMC design is to determine such control input u that will push the system from some initial state to a selected sliding manifold given by $\sigma(\mathbf{z}, t) = 0$ [89]. Furthermore, after the system states reach the sliding manifold, then the control must robustly constrain the system motion on this sliding manifold despite the disturbances acting on the system. Here, $\sigma(\mathbf{z}, t)$ refers as a switching function or a sliding variable that is often selected as a linear combination of systems states and time-variant reference $r(t)$, e.g.,

$$\sigma(\mathbf{z}, t) = r(t) - \mathbf{g}^T \mathbf{z}, \tag{24}$$

with a constant gain vector $\mathbf{g}^T = [g_1, \ldots, g_{n-1}, 1]$ defining asymptotically stable system dynamics on the selected sliding manifold. The control with discontinuities on the sliding manifold,

$$u = \begin{cases} u^+, & \sigma(\mathbf{z}, t) > 0 \\ u^-, & \sigma(\mathbf{z}, t) < 0 \end{cases}, \tag{25}$$

can enforce constraint system sliding motion on the selected manifold, i.e., sliding mode, if u^+ and u^- are selected such that the derivative of the Lyapunov function candidate $L = \sigma^2/2$ is a negative definite, i.e., $\dot{L} = \sigma\dot{\sigma} < 0$. The robust SMC design can be performed by the equivalent control method [89]. It determines the equivalent control u_{eq} as a solution of $\dot{\sigma}\big|_{\sigma=0} = 0$. Then we select u^+ and u^- as continuous functions of the system states, respectively, such that $u^+ > u_{eq} > u^-$. However, such switching control causes unwanted chattering in practical implementations. Therefore, we seek a suitable solution to somehow smooth the control signal and maintain the practical robustness simultaneously. The idea is to perform the SMC design in terms of the control function derivative, in order to eliminate discontinuities on the control signal itself. In this case, the actual control, being the integral of the high-frequency switching function, becomes a continuous function, which leads to chattering attenuation [101]. Similar to in [108], we augment the original system with an additional system state such that it yields

$$\dot{z}_j = z_{j+1}, \dot{z}_n = f(\mathbf{z}) + b(\mathbf{z})u - d, \dot{u} = v. \tag{26}$$

In order to achieve chattering attenuation we introduce the auxiliary sliding variable σ_a as

$$\sigma_a = \dot{\sigma} + \lambda\sigma. \tag{27}$$

Then we can perform the SMC design by σ_a achieving a robust system motion on the auxiliary sliding manifold $\sigma_a = 0$. The original sliding mode will occur only by asymptotic convergence as $\dot{\sigma} + \lambda\sigma = 0$. However, the control u will be a continuous function of time. By the application of the equivalent control method, we can derive control v by, e.g.,

$$v = \begin{cases} v^+, & \sigma_a > 0 \\ v^-, & \sigma_a < 0 \end{cases}, \tag{28}$$

where $v^+ > v_{eq} > v^-$ with the equivalent control v_{eq} derived from the condition $\dot{\sigma}_a = 0$, such that $\sigma_a\dot{\sigma}_a < 0$ [89,101]. Then, we can obtain the continuous control signal u, which is derived by the integration of v:

$$u = \int v dt. \tag{29}$$

Thus, we can achieve chattering attenuation. However, if the discontinuous control in Equation (28) can be implemented in practical systems, small oscillations will still occur [101]. Full chattering elimination is possible by some smooth control. The price that is to be paid in this case is related to deteriorated robustness.

In this paper, we utilize the asymptotic reaching law $\dot{\sigma}_a = -D\sigma_a$. Then, we may consider control v consisting of the equivalent control and the other, which provides the attraction of the selected sliding manifold:

$$v = v_{eq} + D\sigma_a. \tag{30}$$

The equivalent control v_{eq} requires complete information about systems dynamics, including model uncertainties that are not known in practice. Therefore, we replace it with its estimated value $\hat{v}_{eq}$, which is constructed based on a nominal model only, and the rest is considered unknown system perturbation and disturbance. If we furthermore consider Equation (29), then the control u is derived as follows:

$$u = \hat{u}_{eq} + D\int \sigma_a dt. \tag{31}$$

This control law has two components. One represents the estimation of the equivalent control, which is based on the available model knowledge. Another can be referred to as a robustifying control term that involves the disturbance estimation and provides the convergence to the selected sliding mode manifold. Some implications of the smooth control in Equation (31) are further discussed in [108].

Force Control

In order to design a robust force control for the system given by Equations (11) and (1), we define the sliding variable in the dimension of acceleration:

$$\sigma_a = \ddot{x} - \ddot{x}^c, \tag{32}$$

where $\ddot{x}^c$ is the so-called control acceleration. The design of the control acceleration is linked to a specific control objective. In this paper, it is derived from the desired impedance relation (Equation (21)) as follows:

$$\ddot{x}^c = \frac{f^r - f_h}{m_m^d} - k_v\dot{x}, \tag{33}$$

where $k_v = b_m^d / m_m^d$ is an arbitrary chosen velocity feedback gain required for realization of the closed-loop damping, if necessary. Note that, in sliding mode $\sigma_a = 0$, thus we may consider $\ddot{x} = \ddot{x}^c$. Then we can derive from Equation (33):

$$m_m^d\ddot{x} + b_m^d\dot{x} = f^r - f_h, \tag{34}$$

and the resulted impedance transfer function matches Equation (21).

We design the robust control law following the SMC design procedure presented in the previous subsection. We consider f_m in Equation (11) as the system control input in force dimension, and then define the auxiliary control signal u in the acceleration dimension as

$$u = \frac{f_m}{m_m}. \tag{35}$$

In the following, we combine Equations (11) and (32) to yield

$$\dot{u} - \frac{d}{dt}\left(\frac{f_h + f^{dist}}{m_m} + \ddot{x}^c\right) = -D\sigma_a. \tag{36}$$

Now, we seek a control signal u such that its time derivative will fulfill Equation (36). It can be derived as follows:

$$u = \ddot{x}^c + \frac{f_h + f^{dist}}{m_m} - D\int \sigma_a dt. \tag{37}$$

In this case, the control signal u resolves Equation (36) perfectly. However, u assumes knowledge of the unknown disturbance force f^{dist}, and the external force f_h must also be taken into account. They may be dropped from the control due to the robustifying control term, which, we assume, is able to provide their effective estimation. The next consideration is related to the acceleration signal, which is considered unavailable in most practical control applications; however, it is contained in the definition of the sliding variable σ_a. Since the robustifying control term in Equation (37) is computed by the integration of σ_a, it may be resolved in such a way that the necessity for the acceleration measurement simply disappears. Then, the control u can be redesigned such that it finally yields the force control f_m:

$$f_m = m_m \left[\ddot{x}^c + D \left(\int \ddot{x}^c dt - \dot{x} \right) \right], \tag{38}$$

where the control acceleration $\ddot{x}^c$ is given by Equation (33).

The control law proposed in this paper is given by Equations (38) and (33). It is a two-degrees-of-freedom control architecture. The control acceleration from Equation (33), along with the parameters m_m^d and b_m^d of the desired impedance, are related to force control. The robustifying gain D from Equation (38) is related to disturbance suppressing, such that the acceleration sensitivity transfer function can be derived as follows:

$$G_a^s(s) = \frac{s}{s+D}, \tag{39}$$

and the acceleration dynamics can then be written as

$$\ddot{x} = \ddot{x}^c - G_a^s(s) \frac{f_h + f^{dist}}{m_m}. \tag{40}$$

If we further consider the force control given by Equation (33) and

$$f_h = Z_h x, \tag{41}$$

where the human impedance Z_h is given by Equation (1), then it is easy to derive the closed-loop transfer function such that it reads as

$$G_f(s) = \frac{Z_h(s)}{(m_m^d s^2 + b_m^d s) + (1 + \frac{m_m^d}{m_m} G_a^s(s)) Z_h(s)} \tag{42}$$

and the force sensitivity transfer function is

$$G_f^s(s) = \frac{m_m^d}{m_m} G_f(s) G_a^s(s), \tag{43}$$

such that output force in the Laplace domain reads as

$$F_h(s) = G_f(s) \left[F^r(s) - \frac{m_m^d}{m_m} G_a^s(s) F^{dist}(s) \right]. \tag{44}$$

In an ideal case, if the robustifying term in Equation (38) rejects the disturbance perfectly and compensates for the external force such that $\sigma_a = 0$, then $\ddot{x} = \ddot{x}^c$ may be adopted. Thus, the internal control loop may be considered as an acceleration controller. Furthermore, $G_f(s)$ converges to the ideal transfer function described by Equation (22), and $G_f^s(s) \to 0$, then the interaction force can be regulated by the desired impedance (Equation (21)). The control block scheme, which additionally includes generation of reference force by the haptic patterns, is depicted in Figure 9.

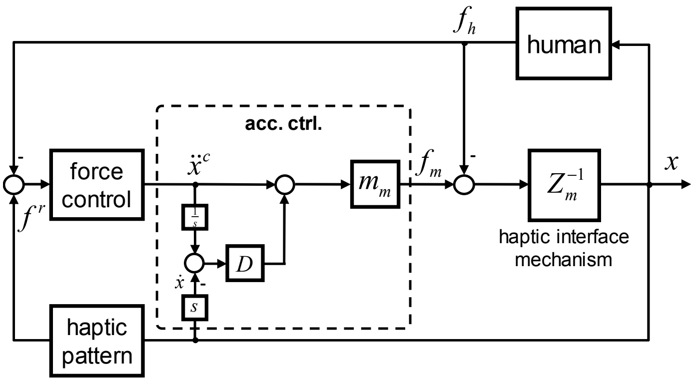

Figure 9. The control block scheme of the haptic interface.

2.5. The Experimental System

The experimental system of the haptic interface for the power lever is shown by the photo in Figure 10. It is designed as a back-drivable impedance type kinesthetic haptic interface with a linear working range of 150 mm. The proposed closed-loop control algorithm requires the external force information. Conventionally, it can be provided by a force or a torque sensor. Alternatively, it can be obtained by the observer-based approach [42,107,145–152]. The latter requires a precise mechanical design, and, furthermore, it cannot compensate for modeling errors and uncertainties that, in sequence, impairs haptic fidelity. Therefore, we employ a force sensor, which is mounted in the handle of the manipulandum. Furthermore, in order to provide rendering of high-fidelity haptic patterns, we additionally apply a precise position encoder.

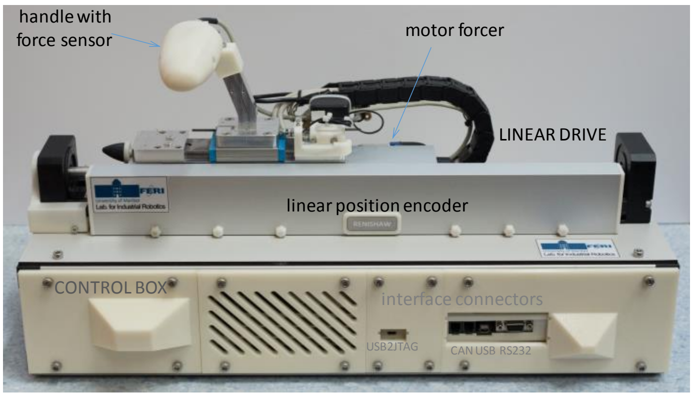

Figure 10. The photo of the experimental haptic interface for power lever.

The main components of the system are: (i) A cogging-free linear brushless servo motor Dunkermotoren STB1116, which consists of a motor forcer and a magnetic rod; it can produce a continuous stall force of ca. 20 N; it is driven by the servo amplifier Copley Controls Accelnet Micro Panel ACJ-055-18-S configured in the current control mode, (ii) a linear position encoder Renishaw VIONiC+RTLC20, which consists of a linear scale and a reading head; it can provide 0.1 um position resolution, (iii) A Burster 8511-5020force sensor with Burster amplifier 9235 was used to measure the applied force by a human hand on the lever handle, and (iv) a haptics controller based on the digital signal processor TI TMS320F28335. A detailed description of the in-house designed haptics controller can be found in [153]. All the control components are placed in the control box below the linear drive.

The connection scheme of the experimental haptic interface is shown in Figure 11. The force sensor, which is mounted in the lever handle, is connected to the haptics controller by a 12-bit analog input via a low-pass analog prefilter with a cutoff frequency of 200 Hz. The position is measured with a precise linear position encoder, which is connected to the dedicated digital quadrature decoder input of the haptics controller. The velocity is estimated from the position counts by the MT method [154]. In order to remove the residual noise, the estimated velocity is filtered by a discretized version of the fast low-pass first-order filter given transfer function $G_v(s) = 1/(\tau s + 1)$, with $\tau = 1$ ms. The control algorithm is executed on the haptics controller at the sampling period of $T_{samp} = 0.1$ ms. The haptics controller also provides the haptic patterns, which output the reference force trajectory. The control output of the control algorithm is converted to the reference current for the servo amplifier, which is transmitted to the servo amplifier by a digital PWM signal. The servo amplifier powers the linear motor, which is mounted on the drive frame with bearing rail.

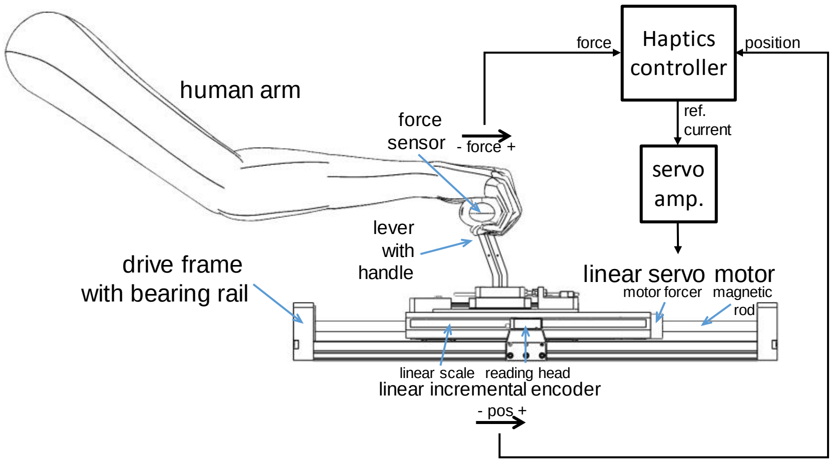

Figure 11. The experimental haptic interface connection scheme.

3. Results

The experimental results shown in this paper aim to verify the proposed control design with the back-drivable impedance haptic interface. In more detail, objective of the experimental verification is to test, if it is possible to provide high-fidelity rendering of the spatially defined haptic patterns by the control algorithm, which has been derived by the chattering-free SMC approach based on the rather simple control plant model. The control algorithm should robustly reject all the model uncertainties and perturbations. Moreover, it should provide good following of the actual force to the reference force trajectories generated by the haptic patterns, i.e., it should provide minimal force error. Nevertheless, the experiments should confirm the enhanced implementation of the control algorithm, and the haptic patterns' algorithms designed for natural feel, especially of the friction haptic pattern.

The experiments were conducted such that the operator performed movement forth and back of the haptic interface lever holding its handle firmly by hand. During motion at moderate to relatively high speed, the control system generated a selected haptic pattern. We mainly observe the movement velocity, the reference and actual force, and the force error, and thus experimentally tuned the control parameters. We use the force error trajectory to evaluate the control performance. It should provide well-damped error response with lowest possible magnitude. Furthermore, the operator feel was also considered in the design of the haptic patterns' parameters.

We tune the control parameters of the control algorithm given by Equations (33) and (38). We focus on the robustifying gain D, and the desired mass m_m^d, and the other control parameters are fixed. In tuning of the control parameters, we consider the following principles. The robustifying gain D adjust robustness of the inner control loop. Higher the value better is robustness. However, in practice this parameter's value is upper bounded due to the factors such as neglected parasitic dynamics, measurement noise, and discrete control implementation. Thus, the optimal value, which shall provide good disturbance rejection while maintaining oscillation-free response, is to be decided experimentally. In case of the desired mass m_m^d, we consider that the lighter the haptic interface moving part, the better the force following. Thus, the desired mass is to be lowered as much as possible. However, similarly as in case of the control parameter D, its value is lower bounded in practical feedback control systems. Therefore, the optimal value should be determined experimentally such that we provide lowest possible force tracking error while maintaining oscillations free response. The values of the control parameters, which apply in the shown experimental results, are written in Table 1.

Table 1. The control parameters.

Parameter	**Value**	**Unit**
m_m	1.8	(kg)
D	100–1000	(s^{-1})
m_m^d	1.8–0.5	(kg)
b_m^d	0	(Ns/m)

The nominal mass inertia of the system m_m was estimated based on a CAD model of the real system. In our experiments, we emphasized high-fidelity haptic rendering, thus we set $b_m^d = 0$, since otherwise it adds an additional damping in the force feedback, which is undesired if it is not required for closed-loop stabilization.

The parameters' values of the applied haptic patterns were determined experimentally in order to obtain good and natural-like feel, as decided by the human operator. The general force level was 10 N, and other parameters specific to certain haptic pattern were as follows:

- Friction: $F_c = 10$ N, $F_s = 10.2$ N, $b_v = 0$ Ns/m, $\delta v = 5$ mm/s, and $K_{vs} = 10$ N/mm;
- Bump: $F_b^{\max} = 10$ N, $p_b = 75$ mm, and $w_b = 4$ mm;
- Graininess: $F_g^{\max} = 10$ N, and $w_g = 4$ mm.

We present the experimental results as follows: Firstly, we show the results of tuning of the robustifying gain D of the internal control loop, which should remove the system disturbance (friction, external force, etc.). The reference force was generated by the CRF haptic pattern (Figure 12), and the friction force pattern (Figure 13), respectively. The diagrams in Figures 12 and 13 show the following traces: (i) The top diagram depicts velocity (blue line), (ii) The diagram in the middle depicts the reference force (green line) and the measured force (pink line), and (iii) The bottom diagram depicts force error (pink line). The results show an effective disturbance compensation. This is best demonstrated at velocity reversals when the own friction of the mechanism changes its sign rapidly. Though some force error can be observed at the low value of D = 100 rad/s, the force error practically disappears at the high value of D = 1000 rad/s. Further increase of the gain value leads gradually to oscillations in the force response. The error peaks remain when the force reference changes extremely rapidly, especially in the case of step changes in the CRF.

Secondly, we show the results of tuning of the force feedback gain given by the desired mass m_m^d of the outer control loop, which should lower the force error in general. Here, the reference force was generated by the bump haptic pattern (Figure 14), and the graininess pattern (Figure 15), respectively. The diagrams of Figures 14 and 15 show the traces similar to Figures 12 and 13: (i) The top diagram depicts velocity (blue line), (ii) The diagram in the middle depicts the reference force (green line) and the measured force (pink line), and (iii) The bottom diagram depicts force error (pink line). We can observe good force following the highly dynamic reference trajectory, especially at the low value of the desired mass ($m_m^d = 0.5$ kg), i.e., at the apparent light-weight haptic interface. Further decrease of this parameter led gradually to oscillations in the force response.

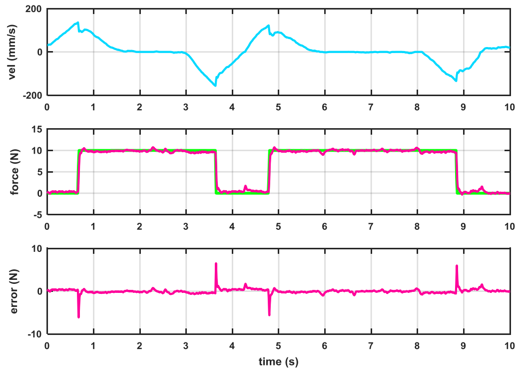

(**a**)

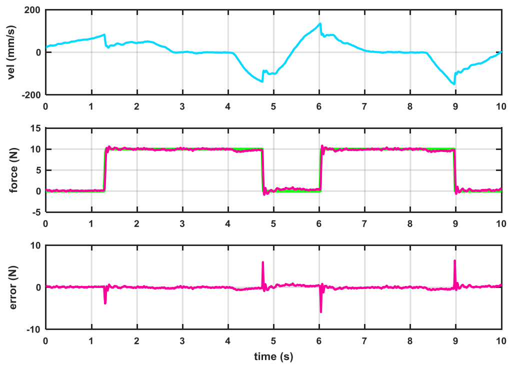

(**b**)

Figure 12. The control response at the CRF ($m_m^d = 1.8$ kg): (**a**) D = 100 rad/s, (**b**) D = 1000 rad/s.

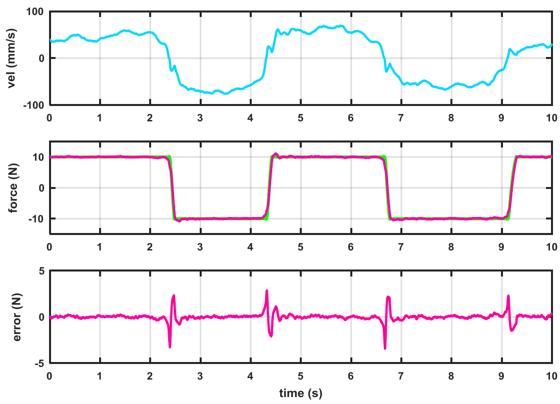

(**a**)

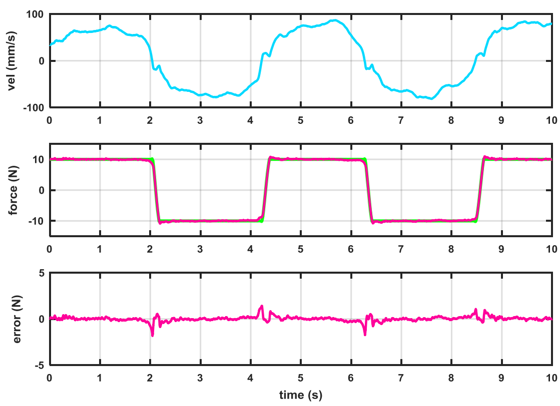

(**b**)

Figure 13. The control response at the friction force ($m_m^d = 1.8$ kg): (**a**) D = 100 rad/s, (**b**) D = 1000 rad/s.

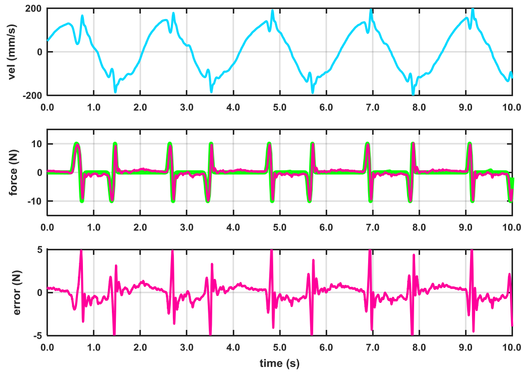

(**a**)

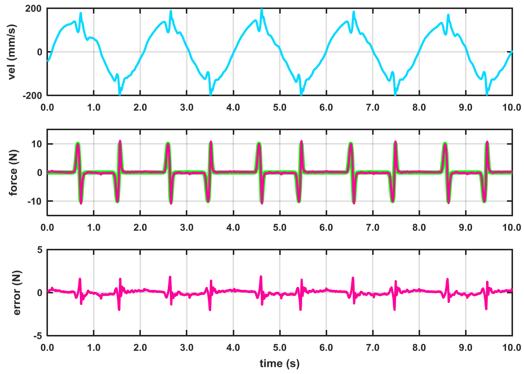

(**b**)

Figure 14. The control response at the bump (D = 1000 rad/s): (**a**) $m_m^d = 1.8$ kg, (**b**) $m_m^d = 0.5$ kg.

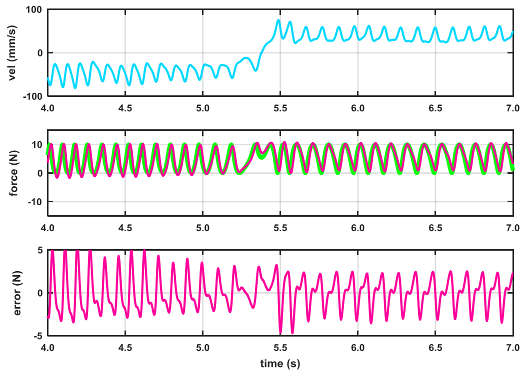

(**a**)

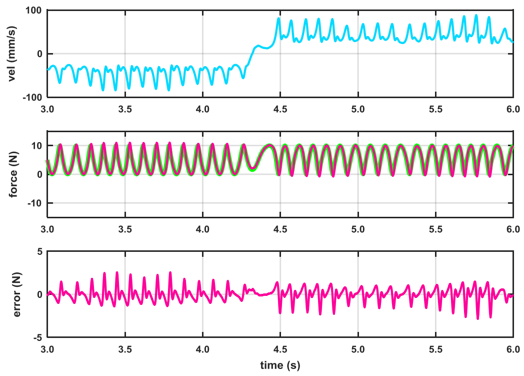

(**b**)

Figure 15. The control response at the graininess (D = 1000 rad/s): (**a**) $m_m^d = 1.8$ kg, (**b**) $m_m^d = 0.5$ kg.

Finally, Figure 16 shows the control results with the optimal control gains found by the previous tuning procedure (D = 1000 rad/s, $m_m^d = 0.5$ kg). Here, the reference trajectory is given by the CRF haptic pattern (Figure 16a), and by the friction force haptic pattern (Figure 16b). The diagrams of Figure 16 show the following traces: (i) The top diagram depicts velocity (blue line), (ii) The diagram in the middle depicts the reference force (green line) and the measured force (pink line), and (iii) The bottom diagram depicts control force, i.e., the force should be generated by the motor (scarlet line). We can observe almost excellent force tracking, with some short interval oscillations at the step changes in the case of the CRF. The bottom diagram illustrates the motor force. It involves several components: (i) The force component, which opposes the human arm, thus, this relates to the negative reference force, and (ii) The force component that should compensate own friction in the mechanism, which changes its sign corresponding to the velocity sign. The dynamics related to the last component are, interestingly, demonstrated on Figure 16a in the case of CRF in the time intervals 2–3 s, and 6.5–7.5 s, respectively. Here, the motion is very slow, about zero velocity, but its direction fluctuates; however, the measured force remains very close to the reference that demonstrates clearly the effectiveness of the proposed control algorithm designed by the SMC approach.

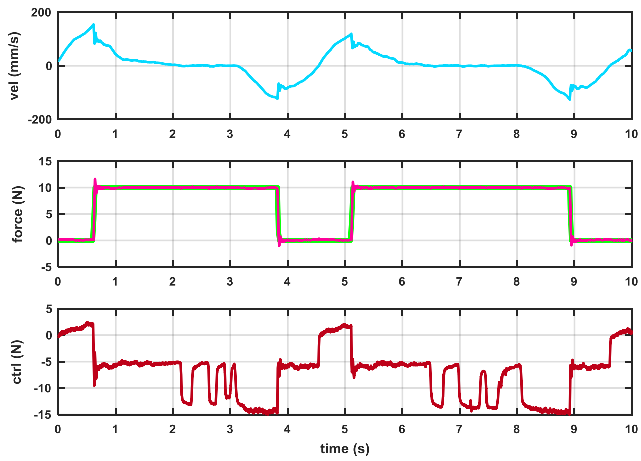

(a)

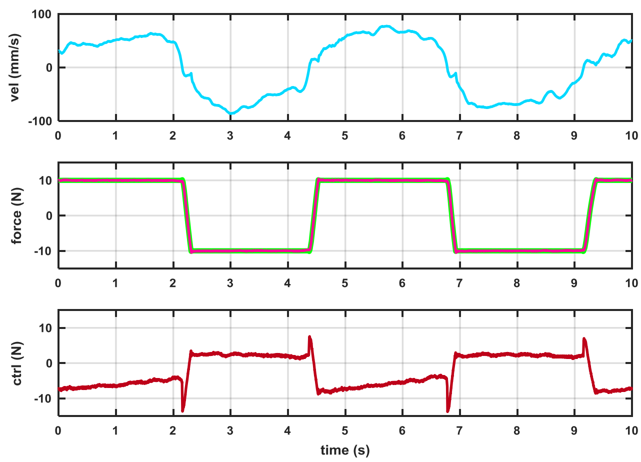

(b)

Figure 16. The control response with the optimal control gains (D = 1000 rad/s, $m_m^d = 0.5$ kg): (**a**) Constant return force; (**b**) friction force.

4. Discussion

The shown experiments verified clearly the proposed control algorithm designed by the SMC approach. Chattering free operation has been proven by practical experiments. Fair robustness performance has also been demonstrated. The key parameter is the robustifying gain of the internal control loop, whose job is to desensitize the closed loop to disturbances. Higher value of the gain assures less influence of the disturbance and faster asymptotic dynamics of the disturbance rejection. However, an upper bound of the gain value is limited in practice—it is typically adjusted as high as determined by the stability of the interface. Note that a high control rate and the quality of the velocity estimation are highly important in this issue. Thus, the advanced MT velocity estimation with minimal phase lag contributes to the relatively high robustness shown in the experiments. Furthermore, the proposed force control with the enforced desired impedance has provided a lightweight and almost friction-less mechanism appearance in the free drive mode with no haptic pattern activated. Thus, the force error was rather low at the optimal control parameters' values, as shown by the experiments.

In our control setup, we applied a force sensor for acquiring the applied human force. An alternative approach could be force estimation by some external force observer, which decreases cost and simplifies the mechanical design significantly. However, this approach requires the availability of an accurate system model to compensate for undesired force components. Accuracy of the force estimation is dependent upon the model employed. Any errors in the model would appear as a part of force estimates from the observer. If a considerable friction is present in the haptic interface mechanism, then the satisfactory model is hard to obtain, since friction is a complex phenomenon, it is non-linear, and the model parameters may be subject to changes during the operation. If friction is not perfectly compensated in the external force observer, then it impairs performance of the haptic interface and haptic fidelity is deteriorated. The same is true if other force components related to system model uncertainties cannot be well compensated. Thus, in our design, we have employed the force sensor instead of the attractive and promising force observer solution. However, with an effective on-line identification algorithm optimized for real-time processing at a high control rate, which could provide, e.g., both dynamic and static friction components accurately, one could benefit significantly by removing the force sensor from the system design in such a high-fidelity application. Thus, future research in this direction is highly desired.

The designed haptic patterns have been rendered by the haptic interface as it has been demanded. The friction algorithm requires a precise position measurement and precise and smooth velocity data. On the other hand, the bump pattern and the graininess pattern are defined spatially; however, during the practical operation, the corresponding reference force trajectory is generated in a time domain that, even at normal human arm speed, may produce relatively high-frequency components in the produced signal. Rendering of haptic patterns such as graininess and bump with the frequency components beyond the bandwidth of the closed-loop force control cannot be optimal. However, our control design demonstrated rather good performance in rendering dynamic haptic patterns. Yet, larger force tracking error in overspeed occurred, as expected, e.g., if we doubled the speed from 50 mm/s to 100 mm/s, then force following was slightly deteriorated at the graininess pattern and the bump pattern; however, this only means slightly lower level of haptic fidelity, the force feedback that was felt remained similar. Similarly, in step change of a CRF haptic pattern, slight transient oscillations occurred at the so-called optimal control parameters' values. Such step change is simply too steep for such control setup. Besides, such step change is not optimal for human haptic perception as well. Therefore, it should be adapted suitably. In the future, the proposed haptic patterns should be fine tuned by a proper psychophysical evaluation in a real environment.

The capabilities of a human to grasp are extremely versatile. We can distinguish different kinds of grasp: a power grasp, a strong power grasp, a weak power grasp, etc. The human impedance also adapts accordingly. We performed numerous experiments in which it was impossible to provide exact repeatability of human arm postures, muscle contractions, and grasps, all of which affect the human arm impedance, which is involved in the control loop. However, the control results with our back-drivable haptic interface were always very similar, with good performance. Thus, relatively high robustness to variable human arm impedance was also demonstrated in our experiments, which proves the effectiveness of the implemented control algorithm. Nevertheless, in order to improve the control performance further, alternative human modeling approaches allowing better representation and prediction of the human operator response such as described in [155,156] may be considered.

5. Conclusions

The haptic power lever has been designed conceptually, in order to communicate relevant information of the aircraft hybrid electric powertrain system to a pilot via human haptics. It enables the pilot to add/drop power of the propeller, and it generates feedback information by force feel with the pilot's hand on the control lever. Thus, the information can be transmitted without requiring the pilot's visual attention; however, hand-on-stick is a required mode of operation in this case. The lever can warn the pilot of the powertrain status, thus enabling a timely pilot response. It contributes to easy and safe use, and promotes efficient energy use. In this paper, we have focused on the control design that is an important issue for high haptic fidelity. The presented experiments demonstrated high effectiveness of the proposed control algorithm and high-quality rendering of the designed haptic patterns. In the future, the haptic power lever shall be designed for practical implementation in the target aircraft and tested in a real environment.

Funding: This work was supported financially by the Slovenian Research Agency (Research Core Funding No. P2-0028), and by funding from the European Union's Seventh Framework Programme for research, technological development and demonstration under Grant Agreement no. 605305 (HYPSTAIR project).

Acknowledgments: The author would like to thank Mitja Golob for assistance in the system design, and for his efforts in programming, performing the experiments, and preparing some graphics. The author would also like to thank former research associate Milan Čurkovič for his valuable technical assistance with the hardware design.

Conflicts of Interest: The author declares no conflict of interest.

References

1. Varga, B.O.; Sagoian, A.; Mariasiu, F. Prediction of electric vehicle range: A comprehensive review of current issues and challenges. *Energies* **2019**, *12*, 946. [CrossRef]
2. Berger, R. Aircraft electrical propulsion—The next chapter of aviation? *Think:Act*, 10 October 2017.
3. Berger, R. Aircraft electrical propulsion—Onwards and upwards. *Think:Act*. July 2018. Available online: https://www.rolandberger.com/publications/publication_pdf/roland_berger_aircraft_electrical_propulsion_2.pdf (accessed on 1 August 2019).
4. Bowman, C. Visions of the future: Hybrid electric aircraft propulsion. In *AIAA Aircraft Electric/Hybrid-Electric Power & Propulsion Workshop*; NASA: Salt Lake City, UT, USA, 2016.
5. PIPISTREL. Electric Flight. Available online: https://www.pipistrel-aircraft.com/aircraft/electric-flight/ (accessed on 7 June 2019).
6. Liu, X.; Qin, D.; Wang, S. Minimum energy management strategy of equivalent fuel consumption of hybrid electric vehicle based on improved global optimization equivalent factor. *Energies* **2019**, *12*, 2076. [CrossRef]
7. Han, S.L.; Cui, S.M.; Song, L.W.; Chan, C.C. Electromagnetic analysis and design of switched reluctance double-rotor machine for hybrid electric vehicles. *Energies* **2014**, *7*, 6665–6688. [CrossRef]
8. Lee, G.-S.; Kim, D.-H.; Han, J.-H.; Hwang, M.-H.; Cha, H.-R. Optimal operating point determination method design for range-extended electric vehicles based on real driving tests. *Energies* **2019**, *12*, 845. [CrossRef]
9. Pan, C.; Liang, Y.; Chen, L.; Chen, L. Optimal control for hybrid energy storage electric vehicle to achieve energy saving using dynamic programming approach. *Energies* **2019**, *12*, 588. [CrossRef]
10. Capata, R. Urban and extra-urban hybrid vehicles: A technological review. *Energies* **2018**, *11*, 2924. [CrossRef]
11. Ullah, M.H.; Gunawan, T.S.; Sharif, M.R.; Muhida, R. Design of environmental friendly hybrid electric vehicle. In *International Conference on Computer and Communication Engineering (ICCCE 2012)*; Springer: Kuala Lumpur, Malaysia, 2012; pp. 544–548.
12. Friedrich, C.; Robertson, P. Hybrid-electric propulsion for aircraft. *J. Aircr.* **2015**, *52*, 176–189. [CrossRef]
13. Friedrich, C.; Robertson, P.A. Hybrid-electric propulsion for automotive and aviation applications. *CEAS Aeronaut. J.* **2015**, *6*, 279–290. [CrossRef]
14. Glassock, R.; Galea, M.; Williams, W.; Glesk, T. Hybrid electric aircraft propulsion case study for skydiving mission. *Aerospace* **2017**, *4*, 45. [CrossRef]

15. Bergqvist, P. Hybrid electric aircraft motor powers up. *Flying Magazine*, 19 February 2016.
16. Cipolla, V.; Oliviero, F. Hypsim: A simulation tool for hybrid aircraft performance analysis. In *Variational Analysis and Aerospace Engineering Workshop-Mathematical Challenges for the Aerospace of the Future*; Frediani, A., Mohammadi, B., Pironneau, O., Cipolla, V., Eds.; Springer: Cham, Switzerland; Erice, Italy, 2016; Volume 116.
17. Zhang, R.F.; Xia, B.Z.; Li, B.H.; Cao, L.B.; Lai, Y.Z.; Zheng, W.W.; Wang, H.W.; Wang, W. State of the art of lithium-ion battery soc estimation for electrical vehicles. *Energies* **2018**, *11*, 1820. [CrossRef]
18. Hypstair (EU fp7 Project). Available online: www.hypstair.eu (accessed on 11 June 2019).
19. Gauci, J.; Cauchi, N.; Theuma, K.; Zammit-Mangion, D. Design and evaluation of a touch screen concept for pilot interaction with avionic systems. In Proceedings of the 2015 IEEE/AIAA 34th Digital Avionics Systems Conference (DASC), Prague, Czech Republic, 13–18 September 2015; pp. 1–32.
20. Wang, L.; Wang, Y.; Chen, Y. Survey on introducing touch-screen into civil aircraft cockpit: Opinions of aircraft designers and pilots. In *IET Conference Proceedings*; Institution of Engineering and Technology: London, UK, 2018; pp. 1260–1265.
21. Grunwald, M. *Human Haptic Perception Basics and Applications*; Birkhäuser: Basel, Switzerland; Boston, MA, USA, 2008; p. ix. 676p.
22. Hatzfeld, C.; Kern, T.A. Engineering haptic devices: A beginner's guide. In *Springer Series on Touch and Haptic Systems*, 2nd ed.; Springer: London, UK, 2014; p. 573.
23. Ganesh, G.; Osu, R.; Naito, E. Feeling the force: Returning haptic signals influence effort inference during motor coordination. *Sci. Rep.* **2013**, *3*, 2648. [CrossRef] [PubMed]
24. Hesse, P.; Nielsen, G. *Haptic Signals—139 New and Known Signals*; Danish DeafBlind Association: Aalborg, Denmark, 2018.
25. Moussette, C. *Simple Haptics—Sketching Perspectives for the Design of Haptic Interactions*; Umeå University: Umeå, Sweden, 2012.
26. El Saddik, A.; Orozco, M.; Eid, M.; Cha, J. *Haptics Technologies–Bringing Touch to Multimedia*; Springer: Berlin, Germany; New York, NY, USA, 2011; p. xv. 218p.
27. Jones, L.A. *Haptics*; The MIT Press: Cambridge, MA, USA, 2018.
28. Culbertson, H.; Schorr, S.B.; Okamura, A.M. Haptics: The present and future of artificial touch sensation. *Ann. Rev. Control Robot. Auton. Syst.* **2018**, *1*, 385–409. [CrossRef]
29. Pedemonte, N.; Laliberté, T.; Gosselin, C. Bidirectional haptic communication: Application to the teaching and improvement of handwriting capabilities. *Machines* **2016**, *4*, 6. [CrossRef]
30. Qin, H.; Song, A.; Liu, Y.; Jiang, G.; Zhou, B. Design and calibration of a new 6 DOF haptic device. *Sensors* **2015**, *15*, 31293–31313. [CrossRef] [PubMed]
31. Barrow, A.; Harwin, W. Design and analysis of a haptic device design for large and fast movements. *Machines* **2016**, *4*, 8. [CrossRef]
32. Franco, W.; Maffiodo, D.; De Benedictis, C.; Ferraresi, C. Use of mckibben muscle in a haptic interface. *Robotics* **2019**, *8*, 13. [CrossRef]
33. Gosselin, F.; Ferlay, F.; Janot, A. Development of a new backdrivable actuator for haptic interfaces and collaborative robots. *Actuators* **2016**, *5*, 17. [CrossRef]
34. Mihelj, M.; Podobnik, J. *Haptics for Virtual Reality and Teleoperation*; Springer: Dordrecht, The Netherlands; New York, NY, USA, 2012; Volume 64.
35. Tavakoli, M.; Patel, R.V.; Moallem, M.; Aziminejad, A. *Haptics for Teleoperated Surgical Robotic Systems*; World Scientific Publishing Co. Pte. Ltd.: Singapore, 2008; Volume 1.
36. Kawasaki, H. *Robot Hands and Multi-Fingered Haptic Interfaces—Fundamentals and Applications*; World Scientific Publishing Co. Pte. Ltd.: Singapore, 2015.
37. Pacchierotti, C. *Cutaneous Haptic Feedback in Robotic Teleoperation*; Springer International Publishing: Cham, Switzerland, 2016.
38. van Der Linde, R.Q.; Lammertse, P.; Frederiksen, E.; Ruiter, B. The hapticmaster, a new high-performance haptic interface. In Proceedings of the Eurohaptics Conference, Edinburgh, UK, 8–10 July 2002.
39. Zhang, S.; Fu, Q.; Guo, S.; Fu, Y. A telepresence system for therapist-in-the-loop training for elbow joint rehabilitation. *Appl. Sci.* **2019**, *9*, 1710. [CrossRef]
40. Ohnishi, K.; Mizoguchi, T. Real haptics and its applications. *IEEJ Trans. Electr. Electron. Eng.* **2017**, *12*, 803–808. [CrossRef]

41. Kang Xiang, K.; Chin, P.J.H.; Rahman, H.A.; Yeong, C.F.; Su, E.L.M.; Narayanan, A.L.T. A novel haptic interface and control algorithm for robotic rehabilitation of stoke patients. In Proceedings of the 2014 IEEE Haptics Symposium (HAPTICS), Houston, TX, USA, 24–27 February 2014; pp. 421–426.
42. Yang, C.; Xie, Y.; Liu, S.; Sun, D. Force modeling, identification, and feedback control of robot-assisted needle insertion: A survey of the literature. *Sensors* **2018**, *18*, 561. [CrossRef]
43. Rodríguez, J.-L.; Velázquez, R.; Del-Valle-Soto, C.; Gutiérrez, S.; Varona, J.; Enríquez-Zarate, J. Active and passive haptic perception of shape: Passive haptics can support navigation. *Electronics* **2019**, *8*, 355. [CrossRef]
44. Abbink, D.A.; Boer, E.R.; Mulder, M. Motivation for continuous haptic gas pedal feedback to support car following. In Proceedings of the 2008 IEEE Intelligent Vehicles Symposium, Eindhoven, The Netherlands, 4–6 June 2008; pp. 283–290.
45. Mulder, M.; Mulder, M.; van Paassen, M.M.; Abbink, D.A. Haptic gas pedal feedback. *Ergonomics* **2008**, *51*, 1710–1720. [CrossRef]
46. Bajcinca, N.; Cortesao, R.; Hauschild, M.; Bals, J.; Hirzinger, G. Haptic control for steer-by-wire systems. In Proceedings of the 2003 IEEE/RSJ International Conference on Intelligent Robots and Systems (IROS 2003), Las Vegas, NV, USA, 27–31 October 2003; Volume 2, pp. 2004–2009.
47. Iqbal, J.; Zuhaib, K.; Han, C.; Khan, A.; Ali, M.A. Adaptive global fast sliding mode control for steer-by-wire system road vehicles. *Appl. Sci.* **2017**, *7*, 738. [CrossRef]
48. Kurihara, Y.; Hachisu, T.; Sato, M.; Fukushima, S.; Kajimoto, H. Periodic tactile feedback for accelerator pedal control. In Proceedings of the 2013 World Haptics Conference (WHC), Daejeon, Korea, 14–17 April 2013; pp. 187–192.
49. Bifulco, G.N.; Galante, F.; Pariota, L.; Spena, M.R. A linear model for the estimation of fuel consumption and the impact evaluation of advanced driving assistance systems. *Sustainability* **2015**, *7*, 14326–14343. [CrossRef]
50. García-Canseco, E.; Ayemlong-Fokem, A.; Serrarens, A.; Steinbuch, M. A haptic gearshift interface for cars. In Proceedings of the International Conference EuroHaptics 2010, Amsterdam, The Netherlands, 8–10 July 2010; pp. 315–320.
51. Gaffary, Y.; Lécuyer, A. The use of haptic and tactile information in the car to improve driving safety: A review of current technologies. *Front. ICT* **2018**, *5*. [CrossRef]
52. Morales, J.; Mandow, A.; Martínez, J.L.; Reina, A.J.; García-Cerezo, A. Driver assistance system for passive multi-trailer vehicles with haptic steering limitations on the leading unit. *Sensors* **2013**, *13*, 4485–4498. [CrossRef]
53. Judalet, V.; Glaser, S.; Gruyer, D.; Mammar, S. Fault detection and isolation via the interacting multiple model approach applied to drive-by-wire vehicles. *Sensors* **2018**, *18*, 2332. [CrossRef]
54. Petermeijer, S.M.; Abbink, D.A.; Mulder, M.; de Winter, J.C.F. The effect of haptic support systems on driver performance: A literature survey. *IEEE Trans. Haptics* **2015**, *8*, 467–479. [CrossRef]
55. Girbés, V.; Armesto, L.; Dols, J.; Tornero, J. Haptic feedback to assist bus drivers for pedestrian safety at low speed. *IEEE Trans. Haptics* **2016**, *9*, 345–357. [CrossRef]
56. Jensen, M.J.; Tolbert, A.M.; Wagner, J.R.; Switzer, F.S.; Finn, J.W. A customizable automotive steering system with a haptic feedback control strategy for obstacle avoidance notification. *IEEE Trans. Veh. Technol.* **2011**, *60*, 4208–4216. [CrossRef]
57. Condomines, J.P.; Defay, F.; Alazard, D. Robust impedance active control of flight control devices. *IFAC Proc. Vol.* **2014**, *47*, 8365–8371. [CrossRef]
58. Goodrich, K.; Schutte, P.; Williams, R. Haptic-multimodal flight control system update. In Proceedings of the 11th AIAA Aviation Technology, Integration, and Operations (ATIO) Conference, Virginia Beach, VA, USA, 20–22 September 2011.
59. Perez-Pinal, F.J.; Cervantes, I.; Diaz-Allen, I.; Maldonado, V. Design of a fly by wire technology system for an experimental more electric ultra-light aircraft. In Proceedings of the 2011 IEEE Vehicle Power and Propulsion Conference, Chicago, IL, USA, 6–9 September 2011; pp. 1–5.
60. Schutte, P.C.; Goodrich, K.H.; Williams, R.A.D. Towards an Improved Pilot-Vehicle Interface for Highly Automated Aircraft: Evaluation of the Haptic Flight Control System. In Proceedings of the 4th AHFE International Conference on Applied Human Factors and Ergonomics, San Francisco, CA, USA, 21–25 July 2012.

61. Grünhagen, W.; Müllhäuser, M.; Abildgaard, M.; Lantzsch, R. Active inceptors in FHS for pilot assistance systems. In Proceedings of the 36th European Rotorcraft Forum, Paris, France, 7–9 September 2010.
62. P.E. Pilots will receive haptic feedback. *Professional Engineering Magazine*, 6 August 2014.
63. Roberts, P. *A World First: Civil Certification of BAE Systems' Active Stick Technology*; BAE Sytems: Farnborough, UK, 2018.
64. Ziat, M.; Wagner, S.; Frissen, I. Haptic feedback to compensate for the absence of horizon cues during landing. In *EuroHaptics 2016*; Springer: London, UK, 2016.
65. McGrath, B.; Cox, J.; McKay, J.; Rupert, A. Mission utility of a tactile display in rotary wing operations. In *AHS 71th International Annual Forum*; American Helicopter Society International, Inc.: Virginia Beach, VA, USA, 2015; Volume 2, pp. 1095–1104.
66. D'Intino, G.; Olivari, M.; Geluardi, S.; Fabbroni, D.; Bülthoff, H.; Pollini, L. A pilot intent estimator for haptic support systems in helicopter maneuvering tasks. In Proceedings of the 2018 AIAA Modeling and Simulation Technologies Conference, Kissimmee, FL, USA, 8–12 January 2018.
67. Olivari, M.; Nieuwenhuizen, F.M.; Bülthoff, H.; Pollini, L. An experimental comparison of haptic and automated pilot support systems. In Proceedings of the AIAA Modeling and Simulation Technologies Conference 2014, Atlanta, GA, USA, 16–20 June 2014.
68. Klyde, D.; Ying-Liang, C.; Richards, N.; Cogan, B. Use of active inceptor cueing to mitigate pilot-vehicle system loss of control. In Proceedings of the AIAA Guidance, Navigation, and Control Conference, Minneapolis, MN, USA, 13–16 August 2012.
69. Colonnese, N.; Sketch, S.M.; Okamura, A.M. Closed-loop stiffness and damping accuracy of impedance-type haptic displays. In Proceedings of the 2014 IEEE Haptics Symposium (HAPTICS), Houston, TX, USA, 24–27 February 2014; pp. 97–102.
70. Parthiban, C.; Zinn, M. Performance and stability limitations of admittance-based haptic interfaces. In Proceedings of the 2018 IEEE Haptics Symposium (HAPTICS), San Francisco, CA, USA, 25–28 March 2018; pp. 58–65.
71. Kazerooni, H.; Ming-Guo, H. The dynamics and control of a haptic interface device. *IEEE Trans. Robot. Autom.* **1994**, *10*, 453–464. [CrossRef]
72. Carignan, C.; Cleary, K. Closed-loop force control for haptic simulation of virtual environments. *Haptics-e Electron. J. Haptics Res.* **2000**, *1*.
73. Abdossalami, A.; Sirouspour, S. Adaptive control of haptic interaction with impedance and admittance type virtual environments. In Proceedings of the 2008 Symposium on Haptic Interfaces for Virtual Environment and Teleoperator Systems, Reno, NV, USA, 13–14 March 2008; pp. 145–152.
74. Šabanović, A.; Ohnishi, K. *Motion Control Systems*; John Wiley & Sons (Asia) Pte Ltd.: South Tower, Singapore, 2011.
75. Suzuki, S.; Furuta, K. Adaptive impedance control to enhance human skill on a haptic interface system. *J. Control Sci. Eng.* **2012**, *2012*, 365067. [CrossRef]
76. Wu, Q.; Wu, H. Development, dynamic modeling, and multi-modal control of a therapeutic exoskeleton for upper limb rehabilitation training. *Sensors* **2018**, *18*, 3611. [CrossRef]
77. Karnopp, D. Computer simulation of stick-slip friction in mechanical dynamic systems. *J. Dyn. Syst. Meas. Control* **1985**, *107*, 100–103. [CrossRef]
78. Armstrong-Hélouvry, B.; Dupont, P.; Wit, C.C.D. A survey of models analysis tools and compensation methods for the control of machines with friction. *Automatica* **1994**, *30*, 1083–1138. [CrossRef]
79. deWit, C.C.; Olsson, H.; Astrom, K.J.; Lischinsky, P. A new model for control of systems with friction. *IEEE Trans. Autom. Control* **1995**, *40*, 419–425.
80. Olsson, H.; Åström, K.J.; deWit, C.C.; Gäfvert, M.; Lischinsky, P. Friction models and friction compensation. *Eur. J. Control* **1998**, *4*, 176–195. [CrossRef]
81. Åström, K.J. Control of systems with friction. In Proceedings of the Fourth International Conference on Motion and Vibration Control, Zurich, Switzerland, 25–28 August 1998; pp. 25–32.
82. Hensen, R.H.A.; van de Molengraft, M.J.G.; Steinbuch, M. Frequency domain identification of dynamic friction model parameters. *IEEE Trans. Control Syst. Technol.* **2002**, *10*, 191–196. [CrossRef]
83. Wilhelm, F.; Tamura, T.; Fuchs, R.; Müllhaupt, P. Friction compensation control for power steering. *IEEE Trans. Control Syst. Technol.* **2016**, *24*, 1354–1367. [CrossRef]

84. Bernstein, N.L.; Lawrence, D.A.; Pao, L.Y. Friction modeling and compensation for haptic interfaces. In Proceedings of the First Joint Eurohaptics Conference and Symposium on Haptic Interfaces for Virtual Environment and Teleoperator Systems, Pisa, Italy, 18–20 March 2005; pp. 290–295.
85. Kikuuwe, R.; Takesue, N.; Sano, A.; Mochiyama, H.; Fujimoto, H. Admittance and impedance representations of friction based on implicit euler integration. *IEEE Trans. Robot.* **2006**, *22*, 1176–1188. [CrossRef]
86. Ueberle, M.-W. *Design, Control and Evaluation of a Family of Kinesthetic Haptic Interfaces*; Technischen Universität München: Munich, Germany, 2006.
87. Hogan, N. Controlling impedance at the man/machine interface. In Proceedings of the 1989 International Conference on Robotics and Automation, Scottsdale, AZ, USA, 14–19 May1989; Volume 3, pp. 1626–1631.
88. Hill, M.D.; Niemeyer, G. Real-time estimation of human impedance for haptic interfaces. In Proceedings of the World Haptics 2009—Third Joint EuroHaptics conference and Symposium on Haptic Interfaces for Virtual Environment and Teleoperator Systems, Salt Lake City, UT, USA, 18–20 March 2009; pp. 440–445.
89. Utkin, V.I. *Sliding Modes in Control and Optimization*; Springer: Berlin/Heidelberg, Germany; New York, NY, USA, 1992.
90. Doan, Q.V.; Le, T.D.; Vo, A.T. Synchronization full-order terminal sliding mode control for an uncertain 3-DOF planar parallel robotic manipulator. *Appl. Sci.* **2019**, *9*, 1756. [CrossRef]
91. Kallu, K.D.; Abbasi, S.J.; Khan, H.; Wang, J.; Lee, M.C. Tele-operated bilateral control of hydraulic manipulator using a robust controller based on the sensorless estimated reaction force. *Appl. Sci.* **2019**, *9*, 1995. [CrossRef]
92. Geng, G.; Shen, Q.; Jiang, H. ANFTS mode control for an electronically controlled hydraulic power steering system on a permanent magnet slip clutch. *Energies* **2019**, *12*, 1739. [CrossRef]
93. Bai, R. Adaptive sliding-mode control of automotive electronic throttle in the presence of input saturation constraint. *IEEE/CAA J. Autom. Sin.* **2018**, *5*, 878–884. [CrossRef]
94. Mohd Zaihidee, F.; Mekhilef, S.; Mubin, M. Robust speed control of PMSM using sliding mode control (SMC)—A review. *Energies* **2019**, *12*, 1669. [CrossRef]
95. Svečko, R.; Gleich, D.; Chowdhury, A.; Sarjaš, A. Sub-optimal second-order sliding mode controller parameters' selection for a positioning system with a synchronous reluctance motor. *Energies* **2019**, *12*, 1855. [CrossRef]
96. Derbeli, M.; Barambones, O.; Ramos-Hernanz, J.A.; Sbita, L. Real-time implementation of a super twisting algorithm for PEM fuel cell power system. *Energies* **2019**, *12*, 1594. [CrossRef]
97. Sabanovic, A.; Fridman, L.M.; Spurgeon, S. *Variable Structure Systems: From Principles to Implementation*; The Institution of Electrical Engineers: London, UK, 2004.
98. Young, K.D.; Utkin, V.I.; Ozguner, U. A control engineer's guide to sliding mode control. *IEEE Trans. Control Syst. Technol.* **1999**, *7*, 328–342. [CrossRef]
99. Fridman, L.; Levant, A. Higher order sliding modes as a natural phenomenon in control theory. In *Robust Control via Variable Structure and Lyapunov Techniques*; Garofalo, F., Glielmo, L., Eds.; Springer: Berlin/Heidelberg, Germany, 1996; pp. 107–133.
100. Bartolini, G.; Ferrara, A.; Usai, E. Chattering avoidance by second-order sliding mode control. *IEEE Trans. Autom. Control* **1998**, *43*, 241–246. [CrossRef]
101. Shtessel, Y.; Edwards, C.; Fridman, L.; Levant, A. *Sliding Mode Control and Observation*; Springer Science+Business Media (Birkhauser): New York, NY, USA, 2014.
102. Utkin, V. Discussion aspects of high-order sliding mode control. *IEEE Trans. Autom. Control* **2016**, *61*, 829–833. [CrossRef]
103. Hace, A.; Jezernik, K.; Uran, S. Robust impedance control. In *The 1998 IEEE International Conference on Control Applications*; IEEE: Trieste, Italy, 1998; Volume 1, pp. 583–587.
104. Hace, A.; Jezernik, K.; Sabanovic, A. Improved design of VSS controller for a linear belt-driven servomechanism. *IEEE/ASME Trans. Mechatron.* **2005**, *10*, 385–390. [CrossRef]
105. Hace, A.; Jezernik, K.; Sabanovic, A. SMC with disturbance observer for a linear belt drive. *IEEE Trans. Ind. Electron.* **2007**, *54*, 3402–3412. [CrossRef]
106. Hace, A.; Franc, M. FPGA implementation of sliding-mode-control algorithm for scaled bilateral teleoperation. *IEEE Trans. Ind. Inform.* **2013**, *9*, 1291–1300. [CrossRef]
107. Hace, A.; Franc, M. Pseudo-sensorless high-performance bilateral teleoperation by sliding-mode control and FPGA. *IEEE/ASME Trans. Mechatron.* **2014**, *19*, 384–393. [CrossRef]

108. Hace, A.; Golob, M. Chattering-free sliding mode control algorithm for a haptic throttle lever. In Proceedings of the IECON 2016-42nd Annual Conference of the IEEE Industrial Electronics Society, Florence, Italy, 24–27 October 2016; pp. 6385–6390.
109. Ghaffari, T.K.; Kövecses, J. A high-performance velocity estimator for haptic applications. In Proceedings of the 2013 World Haptics Conference (WHC), Daejeon, Korea, 14–17 April 2013; pp. 127–132.
110. Chawda, V.; Celik, O.; O'Malley, M.K. Evaluation of velocity estimation methods based on their effect on haptic device performance. *IEEE/ASME Trans. Mechatron.* **2018**, *23*, 604–613. [CrossRef]
111. MacLean, K.E. Haptic interaction design for everyday interfaces. *Rev. Hum. Factors Ergon.* **2008**, *4*, 149–194. [CrossRef]
112. Kosuge, K.; Fujisawa, Y.; Fukuda, T. Control of mechanical system with man-machine interaction. In Proceedings of the IEEE/RSJ International Conference on Intelligent Robots and Systems, Raleigh, NC, USA, 7–10 July 1992.
113. Lawrence, D.A. Stability and transparency in bilateral teleoperation. *IEEE Trans. Robot. Autom.* **1993**, *9*, 624–637. [CrossRef]
114. Tsuji, T.; Goto, K.; Moritani, M.; Kaneko, M.; Morasso, P. Spatial characteristics of human hand impedance in multi-joint arm movements. In Proceedings of the IEEE/RSJ International Conference on Intelligent Robots and Systems (IROS'94), Munich, Germany, 12–16 September 1994; Volume 1, pp. 423–430.
115. Speich, J.E.; Shao, L.; Goldfarb, M. Modeling the human hand as it interacts with a telemanipulation system. *Mechatronics* **2005**, *15*, 1127–1142. [CrossRef]
116. Fu, M.J.; Cavusoglu, M.C. Three-dimensional human arm and hand dynamics and variability model for a stylus-based haptic interface. In *2010 IEEE International Conference on Robotics and Automation*; IEEE: Anchorage, AK, USA, 2010; pp. 1339–1346.
117. Kovács, L.L.; Kövecses, J. Dynamics of coupled haptic systems. In *2015 IEEE World Haptics Conference (WHC)*; IEEE: Evanston, IL, USA, 2015; pp. 286–292.
118. Berger, E.J. Friction modeling for dynamic system simulation. *Appl. Mech. Rev.* **2002**, *55*, 535–577. [CrossRef]
119. Richard, C.; Cutkosky, M.R. Friction modeling and display in haptic applications involving user performance. In Proceedings of the 2002 IEEE International Conference on Robotics and Automation, Washington, DC, USA, 11–15 May 2002; Volume 1, pp. 605–611.
120. Lin, M.C.; Otaduy, M.A. *Haptic Rendering: Foundations, Algorithms, and Applications*; A K Peters, Ltd.: Wellesley, MA, USA, 2008.
121. Minsky, M.D.R. *Computational Haptics: The Sandpaper System for Synthesizing Texture for a Force-Feedback Display*; Massachusetts Institute of Technology, MIT: Cambridge, MA, USA, 1995.
122. Robles-De-La-Torre, G.; Hayward, V. Virtual surfaces and haptic shape perception. In Proceedings of the Haptic Interfaces for Virtual Environment and Teleoperator Systems Symposium, ASME International Mechanical Engineering Congress & Exposition 2000, Orlando, FL, USA, 5–10 November 2000.
123. Robles-De-La-Torre, G.; Hayward, V. Force can overcome object geometry in the perception of shape through active touch. *Nature* **2001**, *412*, 445–448. [CrossRef]
124. Hogan, N. Impedance control: An approach to manipulation: Part i—Theory. *J. Dyn. Syst. Meas. Control* **1985**, *107*, 1–7. [CrossRef]
125. Hogan, N. Impedance control: An approach to manipulation: Part ii—Implementation. *J. Dyn. Syst. Meas. Control* **1985**, *107*, 8–16. [CrossRef]
126. Hogan, N. Impedance control: An approach to manipulation: Part iii—Applications. *J. Dyn. Syst. Meas. Control* **1985**, *107*, 17–24. [CrossRef]
127. Yen, S.-H.; Tang, P.-C.; Lin, Y.-C.; Lin, C.-Y. Development of a virtual force sensor for a low-cost collaborative robot and applications to safety control. *Sensors* **2019**, *19*, 2603. [CrossRef]
128. Han, J.-H.; Kim, D.-H.; Hwang, M.-H.; Lee, G.-S.; Cha, H.-R. Active virtual impedance control for sound-following robots to avoid obstacles. *Electronics* **2019**, *8*, 522. [CrossRef]
129. Nadeau, N.A.; Bonev, I.A.; Joubair, A. Impedance control self-calibration of a collaborative robot using kinematic coupling. *Robotics* **2019**, *8*, 33. [CrossRef]
130. Li, C.; Zhang, Z.; Xia, G.; Xie, X.; Zhu, Q. Efficient force control learning system for industrial robots based on variable impedance control. *Sensors* **2018**, *18*, 2539. [CrossRef]
131. Ba, K.; Yu, B.; Gao, Z.; Li, W.; Ma, G.; Kong, X. Parameters sensitivity analysis of position-based impedance control for bionic legged robots' hdu. *Appl. Sci.* **2017**, *7*, 1035. [CrossRef]

132. Chen, C.; Nie, H.; Chen, J.; Wang, X. A velocity-based impedance control system for a low impact docking mechanism (lidm). *Sensors* **2014**, *14*, 22998–23016. [CrossRef]
133. Zhang, T.; Xia, J. Interconnection and damping assignment passivity-based impedance control of a compliant assistive robot for physical human–robot interactions. *IEEE Robot. Autom. Lett.* **2019**, *4*, 538–545. [CrossRef]
134. Ba, K.; Yu, B.; Ma, G.; Zhu, Q.; Gao, Z.; Kong, X. A novel position-based impedance control method for bionic legged robots' hdu. *IEEE Access* **2018**, *6*, 55680–55692. [CrossRef]
135. Jamwal, P.K.; Hussain, S.; Ghayesh, M.H.; Rogozina, S.V. Impedance control of an intrinsically compliant parallel ankle rehabilitation robot. *IEEE Trans. Ind. Electron.* **2016**, *63*, 3638–3647. [CrossRef]
136. Li, Z.; Liu, J.; Huang, Z.; Peng, Y.; Pu, H.; Ding, L. Adaptive impedance control of human–robot cooperation using reinforcement learning. *IEEE Trans. Ind. Electron.* **2017**, *64*, 8013–8022. [CrossRef]
137. Toedtheide, A.; Lilge, T.; Haddadin, S. Antagonistic impedance control for pneumatically actuated robot joints. *IEEE Robot. Autom. Lett.* **2016**, *1*, 161–168. [CrossRef]
138. Pérez-Ibarra, J.C.; Siqueira, A.A.G.; Silva-Couto, M.A.; de Russo, T.L.; Krebs, H.I. Adaptive impedance control applied to robot-aided neuro-rehabilitation of the ankle. *IEEE Robot. Autom. Lett.* **2019**, *4*, 185–192. [CrossRef]
139. Raiola, G.; Cardenas, C.A.; Tadele, T.S.; de Vries, T.; Stramigioli, S. Development of a safety- and energy-aware impedance controller for collaborative robots. *IEEE Robot. Autom. Lett.* **2018**, *3*, 1237–1244. [CrossRef]
140. Devie, S.; Robet, P.; Aoustin, Y.; Gautier, M. Impedance control using a cascaded loop force control. *IEEE Robot. Autom. Lett.* **2018**, *3*, 1537–1543. [CrossRef]
141. Lawrence, D.A. Impedance control stability properties in common implementations. In Proceedings of the 1988 IEEE International Conference on Robotics and Automation, Philadelphia, PA, USA, 24–29 April 1988; Volume 1182, pp. 1185–1190.
142. Newman, W.S. Stability and performance limits of interaction controllers. *J. Dyn. Syst. Meas. Control* **1992**, *114*, 563–570. [CrossRef]
143. Adams, R.J.; Hannaford, B. Stable haptic interaction with virtual environments. *IEEE Trans. Robot. Autom.* **1999**, *15*, 465–474. [CrossRef]
144. Gil, J.J.; Avello, A.; Rubio, A.; Florez, J. Stability analysis of a 1 DOF haptic interface using the routh-hurwitz criterion. *IEEE Trans. Control Syst. Technol.* **2004**, *12*, 583–588. [CrossRef]
145. Gupta, A.; Patoglu, V.; O'Malley, M. Disturbance observer based closed loop force control for haptic feedback. In Proceedings of the 2007 ASME International Mechanical Engineering Congress and Exposition, Seattle, WA, USA, 11–15 November 2007.
146. Katsura, S.; Matsumoto, Y.; Ohnishi, K. Modeling of force sensing and validation of disturbance observer for force control. *IEEE Trans. Ind. Electron.* **2007**, *54*, 530–538. [CrossRef]
147. Sariyildiz, E.; Ohnishi, K. An adaptive reaction force observer design. *IEEE/ASME Trans. Mechatron.* **2015**, *20*, 750–760. [CrossRef]
148. Sariyildiz, E.; Oboe, R.; Ohnishi, K. Disturbance observer-based robust control and its applications: 35th anniversary overview. *IEEE Trans. Ind. Electron.* **2019**. [CrossRef]
149. Hsueh, P.; Chen, J.; Yao, W.; Tsai, M.; Syu, W. Luenberger observer-based impedance control of linear servo motor for a desired haptic system. In Proceedings of the 2013 CACS International Automatic Control Conference (CACS), Nantou, Taiwan, 2–4 December 2013; pp. 140–145.
150. Yano, T.; Ohnishi, K. Force control for a haptic interface system. In Proceedings of the IEEE ICIT '04 2004 IEEE International Conference on Industrial Technology, Hammamet, Tunisia, 8–10 December 2004; Volume 1, pp. 102–107.
151. Liu, T.; Li, C.; Inoue, Y.; Shibata, K. Reaction force/torque sensing in a master-slave robot system without mechanical sensors. *Sensors* **2010**, *10*, 7134–7145. [CrossRef]
152. Kallu, K.D.; Wang, J.; Abbasi, S.J.; Lee, M.C. Estimated reaction force-based bilateral control between 3dof master and hydraulic slave manipulators for dismantlement. *Electronics* **2018**, *7*, 256. [CrossRef]
153. Čurkovič, M.; Pučko, R.; Golob, M.; Hace, A. Two-axis controller for rapid prototyping in robotic applications (in slovene). *Ventil (Ljubljana)* **2017**, *23*, 208–213.
154. Hace, A. The improved division-less MT-type velocity estimation algorithm for low-cost fpgas. *Electronics* **2019**, *8*, 361. [CrossRef]

155. Martínez-García, M.; Gordon, T.; Shu, L. Extended crossover model for human-control of fractional order plants. *IEEE Access* **2017**, *5*, 27622–27635. [CrossRef]
156. Martinez-Garcia, M.; Gordon, T. A new model of human steering using far-point error perception and multiplicative control. In Proceedings of the 2018 IEEE International Conference on Systems, Man, and Cybernetics (SMC), Vienna, Austria, 2–5 July 2018; pp. 1245–1250.